Stem Cell Reports
Article
ISSCR
OPEN ACCESS

Developing Organoids from Ovarian Cancer as Experimental and Preclinical Models

Nina Maenhoudt,[1] Charlotte Defraye,[1] Matteo Boretto,[1] Ziga Jan,[1,2,3] Ruben Heremans,[1,2,4] Bram Boeckx,[5,6] Florian Hermans,[1,7] Ingrid Arijs,[5,6] Benoit Cox,[1] Els Van Nieuwenhuysen,[2,4] Ignace Vergote,[2,4] Anne-Sophie Van Rompuy,[8] Diether Lambrechts,[5,6] Dirk Timmerman,[2,4] and Hugo Vankelecom[1,*]

[1]Laboratory of Tissue Plasticity in Health and Disease, Cluster of Stem Cell and Developmental Biology, Department of Development and Regeneration, KU Leuven (University of Leuven), 3000 Leuven, Belgium
[2]Cluster Woman and Child, Department of Development and Regeneration, KU Leuven, 3000 Leuven, Belgium
[3]Cancer Centre Carinthia, 9020 Klagenfurt, Austria
[4]Gynecology and Obstetrics, University Hospitals Leuven (UZ Leuven), 3000 Leuven, Belgium
[5]Center for Cancer Biology, VIB, 3000 Leuven, Belgium
[6]Laboratory for Translational Genetics, Department of Human Genetics, KU Leuven, 3000 Leuven, Belgium
[7]Department of Morphology, Biomedical Research Institute, Faculty of Medicine and Life Sciences, Hasselt University, 3590 Diepenbeek, Belgium
[8]Translational Cell & Tissue Research, Department of Imaging & Pathology, KU Leuven, 3000 Leuven, Belgium
*Correspondence: hugo.vankelecom@kuleuven.be
https://doi.org/10.1016/j.stemcr.2020.03.004

SUMMARY

Ovarian cancer (OC) represents the most dismal gynecological cancer. Pathobiology is poorly understood, mainly due to lack of appropriate study models. Organoids, defined as self-developing three-dimensional *in vitro* reconstructions of tissues, provide powerful tools to model human diseases. Here, we established organoid cultures from patient-derived OC, in particular from the most prevalent high-grade serous OC (HGSOC). Testing multiple culture medium components identified neuregulin-1 (NRG1) as key factor in maximizing OC organoid development and growth, although overall derivation efficiency remained moderate (36% for HGSOC patients, 44% for all patients together). Established organoid lines showed patient tumor-dependent morphology and disease characteristics, and recapitulated the parent tumor's marker expression and mutational landscape. Moreover, the organoids displayed tumor-specific sensitivity to clinical HGSOC chemotherapeutic drugs. Patient-derived OC organoids provide powerful tools for the study of the cancer's pathobiology (such as importance of the NRG1/ERBB pathway) as well as advanced preclinical tools for (personalized) drug screening and discovery.

INTRODUCTION

Ovarian cancer (OC) is the most lethal gynecological cancer. In more than 80% of patients, the disease is not discovered until advanced stage and metastasis (Narod, 2016). After primary debulking surgery and adjuvant chemotherapy, 70%–80% of the patients show tumor relapse with increasing chemoresistance (Pignata et al., 2017). Most OC cases display an epithelial phenotype (epithelial OC [EOC]), with 75% of the patients diagnosed with high-grade serous OC (HGSOC) of FIGO stage III or IV (i.e., showing extensive metastatic spread) (Jelovac and Armstrong, 2011). HGSOC causes up to 80% of the mortality among OC patients, and thus represents the most outstanding clinical challenge in gynecological oncology. Etiology and site of origin of EOC, whether it is ovarian surface epithelium (OSE) or fallopian tube epithelium (FTE) (or both), are still under intense debate (Kim et al., 2018).

Mechanisms underlying EOC pathobiology are poorly understood, and therapeutic efficiency and patient survival are not significantly improving (Timmermans et al., 2018). Most studies have been done using cancer cell lines that perform poorly in recapitulating histopathological and molecular phenotype of the tumor of origin and of EOC nature in general, thereby lacking clinical translatability (Lengyel et al., 2014). Patient tumor-derived xenografts, growing in immune-deficient mice, better mimic the original tumor but their establishment is inefficient, lengthy, and costly, and is ethically questionable (Sachs and Clevers, 2014). Therefore, more appropriate experimental and preclinical EOC models are needed.

A powerful research tool to model and study human cancer *in vitro* is provided by the innovative organoid technology. Organoids represent *in vitro* self-developing three-dimensional (3D) tissue reconstructions, reproducing key features of the tissue of origin (Clevers, 2016). In recent studies it has been demonstrated that organoids can be developed from multiple divergent cancer types such as colon, prostate, breast, and endometrial cancer. These tumor-derived organoids maintain type- and patient-specific characteristics (Boretto et al., 2019; Gao et al., 2014; Sachs et al., 2018; Van De Wetering et al., 2015). To derive organoids, patients' tumor biopsies are dissociated into fragments and cells, embedded in a 3D extracellular matrix scaffold (such as Matrigel), and cultured in a cocktail of growth and signaling factors, which must be defined and optimized for each individual cancer type.

In the present study, we established organoids from OC that recapitulate disease and patients' tumor characteristics.

Our study independently confirms and expands the recent report by Kopper et al. (2019), although overall derivation efficiency is lower. Importantly, it adds new developed organoid lines to the growing OC organoid biobank, which is an essential impetus to enable the deciphering of the cancer's complex nature, pathogenesis, therapy resistance, and drug sensitivity, and to move the field forward toward more efficient (patient-tailored) treatments.

RESULTS

Establishing Expandable Organoids from EOC

EOC biopsies (predominantly HGSOC; Table 1) were dissociated and cells seeded in OC organoid culture medium-1 (OCOM1; Table S1), the composition of which was based on the medium previously defined to derive organoids from endometrium and endometrial cancer (Boretto et al., 2017, 2019). However, organoid development efficiency was low (33%) and expandability was limited to 1–2 passages (Figures S1A and S1B). Therefore, we systematically tested culture medium components to improve EOC organoid establishment and growth. Reducing the concentration of the transforming growth factor β (TGFβ) pathway inhibitor A83-01, raising the level of nicotinamide, and changing the source of RSPO1 from cell line-conditioned medium to recombinant protein (culture medium referred to as OCOM2; Figure S1A and Table S1) increased the expandability of developed organoid lines (to 3–7 passages; data not shown) but did not improve formation efficiency (Figures S1A and S1B). Further modification of the medium involving (1) omission of basic fibroblast growth factor (bFGF) and FGF10, (2) addition of insulin-like growth factor 1 (IGF1) and hepatocyte growth factor (HGF), known to stimulate growth of OC cell lines (Aune et al., 2011), and (3) reduction of the p38 mitogen-activated protein kinase inhibitor (p38i) SB203580 (OCOM3; Figure S1A and Table S1), shown to be beneficial for establishing organoids from other cancer types such as endometrial and breast cancer (Boretto et al., 2019; Sachs et al., 2018), improved formation efficiency (Figure S1A and S1B) but did not further increase expandability (data not shown). TGFα, reported to induce cell proliferation in cancerous OSE (Sheng et al., 2010), did not advance organoid growth initiation (data not shown), while RSPO1 was found to be essential (Figure S1B; comparable with Kopper et al., 2019 and Hill et al., 2018). Finally, we found that addition of NRG1 (OCOM4; Figure S1A and Table S1) significantly increased the number of organoids formed (Figure S1C), thereby independently (without prior knowledge) confirming, and in addition quantitatively supporting, the recent finding by Kopper et al. (2019). This beneficial effect of NRG1 is also in line with previous studies showing a potential (paracrine) growth-stimulatory effect of NRG1 in OC tumors and cell lines (Gilmour et al., 2002; Sheng et al., 2010). We further zoomed in on the effect of NRG1 and found a significant increase in the number of proliferating ($Ki67^+$) cells in the organoid cultures as well as of the size of the organoids (Figure S1D). Taken together, by thoroughly probing multiple medium components, we eventually defined a culture medium (OCOM4) that strongly enhanced the EOC organoid formation efficiency (from 33% to 56%; Figure S1A). Interestingly, addition of NRG1 also increased the passageability of the EOC-derived organoids (Figure S1E). Although the number of organoids formed at tumor seeding (passage 0 [P0]) in OCOM4 was not inferior to the culture medium used in Kopper et al. (2019) (Figure S1F; "Kopper" medium, see Table S1), overall organoid derivation efficiency over total number of patients remained lower (for a detailed comparison, see Table S2). Possible reasons are described in the Discussion. Of note, organoid formation efficiency did not significantly differ between freshly obtained and cryopreserved biopsies (Figure S1G and Table 1), thereby underscoring the possibility to store clinical samples pending organoid establishment (as described for some other cancers, in particular mouse xenograft and human breast tumors; Walsh et al., 2016). Furthermore, organoids could be derived from EOC biopsies of both chemo-naive patients (obtained by primary debulking surgery) and chemotherapy-treated patients (obtained by interval debulking surgery after prior neoadjuvant chemotherapy) (Figure S1G).

In the culture conditions as optimized above, EOC-derived organoids typically developed within 2–4 weeks, at a rate varying in accordance with individual patients' tumors (Figure 1A). Organoid morphology also differed between patients' EOC samples, displaying either a dense phenotype with no or only small lumen, a disorganized configuration of low cellular cohesiveness ("low-cohesive"), or a cystic phenotype with a (single) cell layer bordering a large lumen (Figure 1B; comparable with Kopper et al., 2019). The different organoid types all showed substantial proliferative activity ($Ki67^+$; Figure 1B) and could be expanded, either short-term (up to 4 passages) or long-term (more than 4 passages, up to 1 year and more) (Figure 1C and Table 1). Although the overall efficiency of establishing organoids from HGSOC patients was lower than that in Kopper et al. (2019), the percentage of long-term passageable organoids among the established lines was comparable (see Table S2). The organoids retained their proliferative activity in later passages without any signs of decreased cell viability (as assessed by immunostaining for the apoptosis marker cleaved-caspase 3; Figure S1E). All organoid lines established were cryopreserved and biobanked (Table 1).

Table 1. Overview of EOC Patients and Samples and of Established Organoid Lines

Patient/EOC Sample No.	Fresh/Cryo	EOC Type[a]	Patient Treatment[b]	EOC Organoid Line[c]	Organoid Morphology	Passaging Time
1	fresh	malignant mixed mesonephric tumor IC2	PDS	–		
2	fresh	HGSOC IVA	IDS	–		
3	fresh	HGSOC IVB	PDS	EOC-0_1	cystic/low-cohesive	short-term
4	fresh	HGSOC IIIC	IDS	EOC-0_2	dense/cystic	long-term
5	fresh	HGSOC IIIC	IDS	–		
6	fresh	HGSOC IVB	IDS	–		
7	fresh	HGSOC IIIC	IDS	–		
8	cryo	HGSOC IVB	IDS	–		
9	fresh	LGSOC IVB	IDS	EOC-0_3	dense/low-cohesive	short-term
10	fresh	HGSOC IVB	TDS	EOC-0_4	dense	long-term
11	cryo	HGSOC IIIC	PDS	–		
12	fresh	HGSOC IIIC	IDS	–		
13A	fresh	HGSOC IVB (omentum)	IDS	–		
13B	cryo	HGSOC IVB (ovary)	IDS	EOC-0_5	dense	short-term
14	fresh	clear cell ovarian cancer IIIA1(i)	PDS	EOC-0_6	dense/cystic	short-term
15	cryo	HGSOC IVB	IDS	EOC-0_7	cystic	long-term
16	cryo	HGSOC IVB	IDS	–		
17	cryo	HGSOC IIIB	SDS	–		
18	fresh	HGSOC IIIC	IDS	EOC-0_8	low-cohesive	long-term
19	fresh	HGSOC IVB	IDS	–		
20	fresh	HGSOC IVB	IDS	–		
21A[d]	*fresh*	*HGSOC IIIC (ovary)*	*IDS*	*EOC-0_9*	*cystic*	*long-term*
21B	fresh	HGSOC IIIC (omentum)	IDS	–		
21C	fresh	HGSOC IIIC (rectum)	IDS	–		
22	cryo	mucinous cystadenocarcinoma IC1	PDS	EOC-0_10	cystic	short-term
23A	cryo	HGSOC IVB (ovary)	PDS	EOC-0_11	cystic	long-term
23B	cryo	HGSOC IVB (omentum)	PDS	–		
24	cryo	HGSOC IVB	IDS	EOC-0_12	dense	short-term
25	cryo	HGSOC IIIC	IDS	–		
26	cryo	LGSOC IIIC	PDS	EOC-0_13	dense/low-cohesive	short-term
27	cryo	HGSOC IIB	PDS	–		

[a]HGSOC, high-grade serous ovarian cancer; LGSOC, low-grade serous ovarian cancer. In case of additional out-of-the-ovary sampling from the same patient, the different surgical sites are specified.
[b]IDS, interval debulking surgery; PDS, primary DS; SDS, secondary DS; TDS, tertiary DS.
[c]–, no organoid derivation.
[d]Eventual healthy tissue organoids.

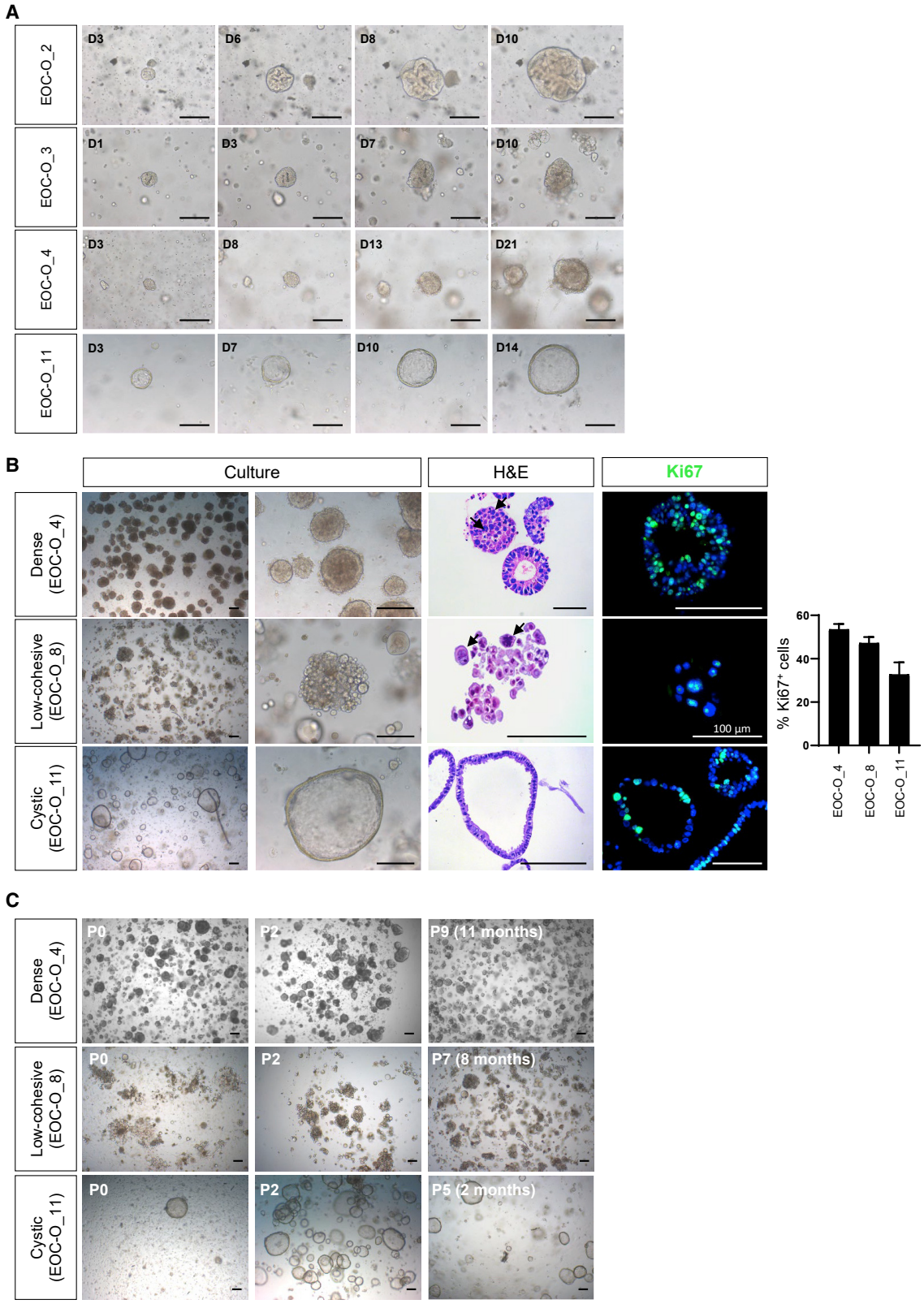

(legend on next page)

EOC-Derived Organoids Reproduce Disease and Original Tumor Phenotype

First, histological (hematoxylin-eosin [H&E]) analysis was performed showing high-grade nuclear atypia in the primary tumor samples as characteristic for EOC (particularly HGSOC) (Figures 2A, 2B, and S2A). High-grade nuclear atypia were also observed in the EOC-derived organoids (Figures 1B, 2A, 2B, and S2A). Moreover, multinucleated giant cells found in the primary tissue were also present in the corresponding organoids (Figure S2A; EOC-O_8). Second, epithelial markers (cytokeratin 8 [CK8], CK18, E-cadherin) were positive in the primary tumor and prominently expressed in the organoids, thereby demonstrating their (tumor) epithelial nature as typical for organoid models (Figures 2A and S2B; Table 2) (Sachs and Clevers, 2014). Third, expression of the HGSOC markers PAX8 (Hardy et al., 2018; Wang et al., 2015) and CK7 (Cathro and Stoler, 2002) was observed in primary tumor, which was effectively recapitulated in the organoids (Figure 2A and Table 2). The tumor-suppressor protein p53 is often mutated in HGSOC (The Cancer Genome Atlas Research Network, 2011) and the p53 immunostaining profile is used for pathological diagnosis. The aberrant p53 overexpression pattern (i.e., intense nuclear staining) in primary tumors was mirrored in corresponding organoid lines (Figure 2B and Table 2). Also, complete absence of p53 immunostaining ("null pattern") in the primary tumor was recapitulated in the derived organoids (Figure 2B, EOC-O_12; Table 2). The expression profile of estrogen receptor α (ERα) and progesterone receptor (PR), clinically variable in HGSOC (Voutsadakis, 2016), was also retained in the corresponding organoid lines (Figure 2A and Table 2). Finally, we performed additional immunohistological and immunofluorescence analyses on organoid lines for which no or insufficient primary tissue was available, and found expression of the HGSOC markers (Figure S2C and Table 2).

Next, we analyzed in organoid lines of different patients/morphology the gene expression of multiple markers known to be highly or lowly expressed in HGSOC (Figure 2C). Organoids showed prominent expression of *CD9*, *CK19*, and *HE4*, the latter being one of the most frequently upregulated genes in EOC (Hwang et al., 2012; Schummer et al., 1999). In contrast, expression levels of *CK20* and *ERβ* (which is highly expressed in normal OSE; Lazennec, 2006) were very low to absent, typical characteristics of EOC (Cathro and Stoler, 2002; Voutsadakis, 2016). *PAX2*, an FTE transcription factor that is lost in 85% of EOC (Hardy et al., 2018), was undetectable in the HGSOC organoid lines (Figure S2D). We also analyzed the expression of the *ERBB* receptor family through which NRG1 acts (Harris et al., 2019). Interestingly, *ERBB2* and *ERBB3* are highly expressed in the organoids, and expression of *ERBB3*, one of the cognate receptors of NRG1, is predominantly enriched in comparison with the primary tumor (Figure 2D). The role and clinical significance of ERBB2 (HER2) and ERBB3 (HER3) in OC remain unclear and controversial. The new EOC organoid models provide experimental tools to revive this field (see Discussion). Comparison of *ERBB* receptor expression in organoids developed with and without NRG1 (OCOM4 and OCOM3, respectively) suggests that the final optimized NRG1-containing culture conditions do not select for an NRG1-dependent (ERBB-expressing) subset among EOC types, since organoids grown in medium without NRG1 (i.e., OCOM3) showed *ERBB* expression levels similar to those of organoids grown in OCOM4 (Figure S2E).

Taken together, patients' EOC-derived organoids reproduce the disease's cellular and molecular phenotype and show atypia and protein marker expression as present in the original tumor.

Patient EOC-Derived Organoids Recapitulate Genomic and Mutational Landscape of the Primary Tumor

We investigated whether the organoid lines also recapitulated the genetic make-up of their parent tumor. Low-coverage whole-genome sequencing revealed that the vast majority of somatic copy-number alterations (SCNA) in primary tumors were retained in the corresponding organoid lines (Figure 2E). These data also allowed to bioinformatically evaluate tumor content of primary biopsy and derived organoids, showing a clear enrichment and high tumor purity in the organoids (Figure 2E). Prominent SCNA were also observed (using array comparative genomic hybridization [array CGH]) in other organoid lines (for which primary tissue was not available; Figure S2F), thereby demonstrating their chromosomally aberrant nature with multiple gains or losses as frequently observed in HGSOC (Kuo et al., 2009; The Cancer Genome Atlas Research

Figure 1. Establishing Organoid Cultures from Ovarian Cancer

(A) Organoid development from EOC (passage 0, P0), showing patients' tumor-associated differences in growth rate. Representative bright-field images are shown at different days (D) after seeding. Scale bars, 200 μm.

(B) Distinct morphology of patients' EOC organoid lines. Representative images of organoid culture and individual organoids (bright-field), of H&E staining, and of Ki67 immunofluorescence analysis (DAPI as nuclear stain) are shown. Some high-grade nuclear atypia are indicated by arrows. Bar graph (right) depicts the proportion of $Ki67^+$ cells in the organoid lines as indicated (mean ± SEM, n = 3–5 independent experiments per line). Scale bars, 200 μm unless indicated otherwise.

(C) Long-term expansion of EOC organoid lines. Representative bright-field images of different passages (P) are shown. Scale bars, 200 μm.

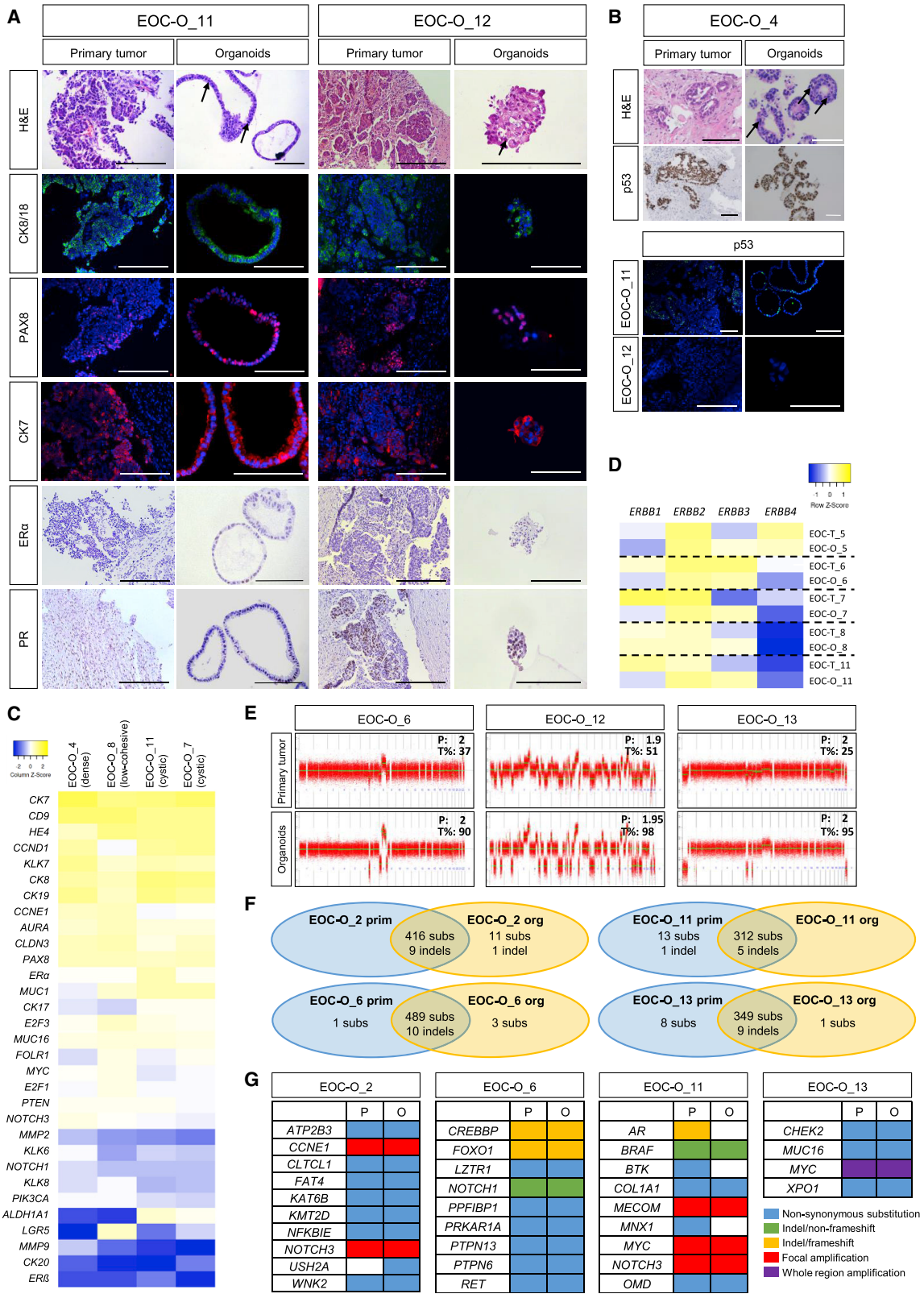

(legend on next page)

Network, 2011) and as found here (Figure 2E). Immunostaining analysis of mutant p53 also supported the major tumor content of these organoid lines (Figure S2F). SCNA present in the primary tissue of EOC-O_9 were not retrieved in the derived organoid culture (Figure S2F), indicating that these organoids developed from non-cancerous epithelial cells present in the biopsy, which overtook the culture (as previously also reported for other cancer-derived organoids; Boretto et al., 2019; Gao et al., 2014; Van De Wetering et al., 2015; Yan et al., 2018), further supported by normal-cell histology (round, polarized) of the organoids and the absence of nuclear atypia and nuclear p53 expression, the latter being present in the primary tissue (Figure S2F). Expression of PAX8 and acetylated α-tubulin point to an FTE origin of this organoid line (Figure S2F; Kessler et al., 2015; Kopper et al., 2019).

Next, several tumors from patients' wild-type for germline *BRCA1* (as retrieved from the patients' pathology reports) were sequenced at the exome base-pair level using whole-exome sequencing (WES), together with the derived organoids. The vast majority (98%) of the genetic alterations detected (i.e., 1,638) were similarly present in both primary tumor and resultant organoid line (Figure 2F and Table S3). In particular, mutations in cancer consensus genes (Sondka et al., 2018), in OC-relevant genes (i.e., genes mutated in >4% of OC; Gao et al., 2013) and in the homologous recombination pathway (Pennington et al., 2014) were identified, which highly corresponded between tumor and organoids (Figure 2G and Table S3). For instance, we found frameshift or non-synonymous mutations in the tumor-suppressor genes *CREBBP*, *FOXO1*, *PRKAR1A*, and *CHEK2* (Toss et al., 2015; Wang et al., 2016; Xie et al., 2012; Zhang et al., 2017), identically in primary tumor and derived organoids. Non-synonymous substitutions in the nuclear transport protein *XPO1*, which regulates export of tumor suppressors, cell-cycle inhibitors, and oncogenes (Azmi et al., 2017), were similarly observed in both tumor and organoids. A non-frameshift insertion and deletion were detected in the key cancer/OC-associated genes *BRAF* and *NOTCH1*, respectively, identically in tumor and corresponding organoids. The loss of three mutations in EOC-O_11 organoids (Figure 2G) may point to a selection of (a) subclone(s) in this particular organoid line (as also reported for other cancer-derived organoids; Boretto et al., 2019; Broutier et al., 2017). Finally, focal or whole-region amplification, as being propelled by central driver genes (*MYC*, *MECOM*, *NOTCH3*, *CCNE1*), was similarly present in tumor and corresponding organoid line (Figure 2G). Of note, WES confirmed the *BRCA1* wild-type genotype of the patients/samples analyzed (as prospectively retrieved from the patients' reports) and also showed a *TP53* wild-type genotype (which, retrospectively, was in agreement with the patients' reports). Developing long-term expandable organoids from patients with high-risk OC predisposition due to a germline *BRCA1* mutation (Antoniou et al., 2003) (Figure S2G) provides new *in vitro* research models that should allow us to investigate the role and impact of *BRCA1* mutation in OC progression.

Taken together, the developed patients' EOC-derived organoids highly recapitulate the genomic constitution of the primary tumor.

EOC-Derived Organoids Show Tumor-Specific Sensitivity to Clinically Used Chemotherapy

To explore the potential of the EOC-derived organoids for *in vitro* drug screening applications, we tested the effect of several chemotherapeutic agents standardly used in the clinic to treat HGSOC (i.e., paclitaxel, carboplatin,

Figure 2. EOC-Derived Organoids Capture Disease and Primary Tumor Phenotype

(A) Organoids reproduce the primary tumor's molecular and cellular phenotype. Representative pictures of H&E staining and immunostaining of disease-associated protein markers in primary tumor and organoids are shown (DAPI and hematoxylin as nuclear stain). The primary tissue shows abundant high-grade nuclear atypia (H&E), which are also found in the organoids (some indicated with arrows). Scale bars, 200 μm.

(B) Organoids reproduce the primary tumor's p53 phenotype. Representative pictures of H&E staining and p53 immunostaining in primary tumor and organoids are shown (DAPI and hematoxylin as nuclear stain). The primary tissue shows abundant high-grade nuclear atypia (H&E), which are also found in the organoids (some indicated with arrows). Scale bars, 200 μm.

(C) Organoids show EOC (HGSOC)-associated gene expression profile. Heatmap of expression of genes, as quantified by qRT-PCR and presented as relative expression to *GAPDH* (ΔC_t) (visualized as color-coded row *Z* score), in organoids from different patients (with different morphology) is shown. Colors range from blue (low expression) to yellow (high expression).

(D) *ERBB* expression profile in primary tumors (EOC-T) and corresponding organoids (EOC-O) as quantified by qRT-PCR and presented as relative expression to *GAPDH* (ΔC_t), visualized as color-coded row *Z* score. Colors range from blue (low expression) to yellow (high expression).

(E) Organoids capture the mutational profile of the primary tissue. Representative copy-number profiles from three different organoid lines (analyzed at P2–P4) and corresponding primary EOC tumor are shown. Numbers indicate ploidy (P) and tumor cell fraction (T%).

(F) Venn diagrams presenting the number of genetic aberrations (subs, substitutions; indel, insertion/deletion) that are common (intersection) or different between primary tumor and corresponding organoids. Numbers were retrieved from Table S3.

(G) Mutation matrix representing hits in cancer consensus, OC-relevant, homology recombination, and amplification-driver genes as detected by WES in primary tumor and derived organoids. P, primary tumor; O, organoids.

Table 2. Overview of Immunohistochemical and Immunofluorescent Analysis of HGSOC-Derived Organoids

	E-cadherin	CK8/CK18	PAX8	CK7	p53	ERα	PR
EOC-O_4	+	+	+	+	+	+/−	+
EOC-O_7[a]	+	+	+	+	−	+/−	+
EOC-O_8	+	+	+	+	+	+/−	+/−
EOC-O_11	+	+	+	+	+/−	−	+/−
EOC-O_12	+	+	+	+	−	−	+

+, positive; +/−, some positive cells; −, no positive cells.
[a]Data not shown.

doxorubicin, and gemcitabine) on established EOC organoids. Drug-response curves revealed distinct sensitivities of the different organoid lines for the drugs (Figure 3), thereby indicating patients' tumor-dependent responses, and at the same time exposed distinct efficacies of the different drugs on individual tumor organoid lines (Figure S3A). Also, nutlin-3 (currently tested as a targeted therapeutic agent for *TP53* wild-type EOC in preclinical settings; Zanjirband et al., 2017) showed different activity depending on the patient's tumor, and more in particular on the p53 status. EOC-O_7 organoids, derived from a *TP53* wild-type tumor (information retrieved from the patients' pathology report), is sensitive to nutlin-3 (Figure S3B). In contrast, EOC-O_4 and EOC-O_8 organoids, established from *TP53* mutant tumors (Figures 2B and S2F; corresponding to the patient pathology reports) showed resistance to nutlin-3 (Figure S3B). Together, our tests show the potential applicability of EOC-derived organoids for drug screening (see also Kopper et al., 2019).

DISCUSSION

In the present study, we established organoids from patients' EOC (predominantly HGSOC). EOC organoid derivation was not negatively influenced by prior cryopreservation of the clinical biopsy, enabling sample collection and storage pending organoid establishment (as also described for some other cancers, in particular mouse xenograft and human breast tumors; Walsh et al., 2016). We found that NRG1 exerts a beneficial effect on EOC organoid development and growth, including increased proliferative activity. Our data, together with the recent findings of Kopper et al. (2019), support an important impact of NRG1 on OC growth (Gilmour et al., 2002; Sheng et al., 2010) and may provide hints toward NRG1-targeted treatment prospects (Drilon et al., 2018). In particular, we found high expression of *ERBB2* (HER2) in tumors and organoids, and high, enriched expression of *ERBB3* (HER3) in the organoids. NRG1 acts through ERBB3 (and/or ERBB4), which heterodimerizes with ERBB2 (Harris et al., 2019). The role and clinical significance of HER2 in OC, in contrast to its proven importance in breast cancer, remain unclear and controversial (Serrano-Olvera et al., 2006). A recent meta-analysis revealed a potential prognostic value, although no association was found for serous OC (Luo et al., 2018). Early preclinical studies have defined HER2 as a potential therapeutic target in OC, but have not extensively been followed up nor translated into clinical practice, particularly because the tested HER2-targeted agents failed to show a significant response (Shu et al., 2017). More recent studies suggest that targeting HER2 (e.g., using trastuzumab) sensitizes OC to chemotherapy (Harris et al., 2019; Shu et al., 2017). Given the success of targeting HER2 in breast and gastric cancer, continuing efforts are recommended regarding HER2 in OC, which can now be explored using the EOC organoid models. Also, the role and significance of ERBB3/HER3 (being one of the cognate receptors of NRG1) in OC remain to be determined. HER3 expression might be associated with worse survival in OC, particularly when HER2 is concomitantly overexpressed (Ocana et al., 2013). A recent study revealed an activated NRG1/ERBB3 pathway in OC cell lines (*in vitro* and as xenograft *in vivo* which, however, showed distinct death or proliferation-block responses), and in a significant fraction (~30%) of patients' advanced-stage OC (as studied using tumor cells from ascites) (Sheng et al., 2010). Similar to HER2, targeting HER3 may also potentiate the effect of chemotherapy (Camblin et al., 2019). The EOC organoid models, developed here and in other studies, may revive this domain to decipher the role, impact, and targetability of the NRG1/ERBB2/ERBB3 pathway in OC. Moreover, patient-derived EOC organoids may help to predict individual patient responses and identify the OC patients who may benefit from NRG1/ERBB2/ERBB3-oriented therapy.

Although the initial development of organoids from the tumor biopsy is comparable in our optimized culture medium OCOM4 and the Kopper medium, overall derivation efficiency is lower than in Kopper et al. (2019). Several variables may account for this difference, including patient group variability and heterogeneity (e.g., not covering identical geno-/phenotypes) and biopsy variability (e.g., regarding quality/necrosis, size, tumor abundance). Furthermore, differences in medium components (such as hydrocortisone and forskolin) may, although not affecting the organoid number at initiation, still be important to enhance the efficiency of kick-starting organoid cultures from individual patients. Extensive comparison with the culture conditions of other recent OC organoid studies (Hill et al., 2018; Maru et al., 2019) was not performed.

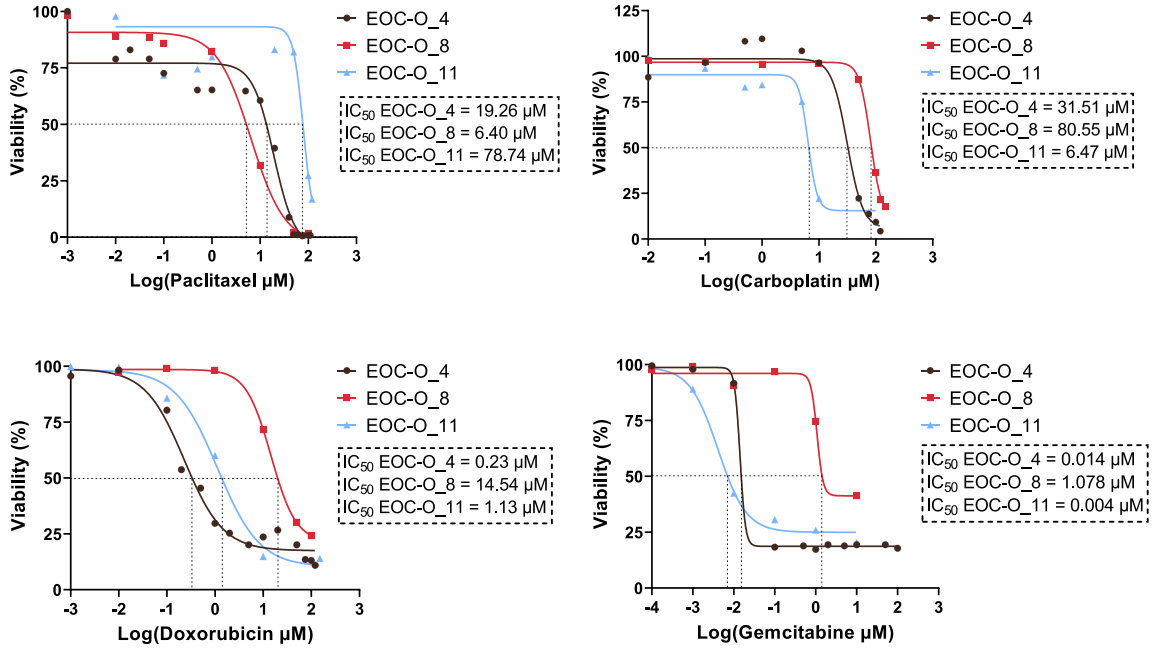

Figure 3. EOC-Derived Organoids Show Patient-Specific Drug Responses

Dose-response curves of EOC organoid cultures from different patients treated for 72 h with drugs are shown. Cell viability was measured using XTT assay. Mean data points (n = 3 biologically independent experiments, i.e., independent donors, with each dot representing the mean of three technical replicates per donor) are displayed for each drug concentration analyzed. IC_{50} values are determined (dashed lines) and indicated.

Despite the now well-demonstrated capacity to establish organoids from EOC, more studies are required to enhance the derivation efficiency (as is also true for other cancer-derived organoids; Boretto et al., 2019; Gao et al., 2014), in particular by scrutinizing and fine-tuning culture conditions to eventually capture more patients and geno-/phenotypes. Although still unsettled and controversial, HER2 overexpression may be present in 10%–30% of all OC types and 20%–40% of HGSOC (which may be higher in advanced stages) (Harris et al., 2019), and HER3 is reported to be expressed in a widely divergent range (from 3% to 90%) of all OC (Davies et al., 2014) and an estimated 20% of serous OC (Rajkumar et al., 1996). It could be possible that our culture conditions (probably also true for Kopper et al., 2019) capture the establishment of organoids from NRG1-dependent (i.e., ERBB-expressing) subtypes of EOC. Although we provide supportive data that the finally optimized culture condition containing NRG1 does not select for NRG1-dependent (ERBB-expressing) OC types, we cannot exclude that initial organoid formation may occur under the influence of endogenous NRG1 (thus indeed thriving ERBB-expressing samples), with exogenous NRG1 enhancing the efficiency by increasing the number of organoids.

The established EOC-derived organoids capture disease cellular characteristics (high-grade nuclear atypia) and molecular phenotype (marker expression). Interestingly, mucin 16 (*MUC16*) was also found to be expressed in the organoids, and non-synonymous substitutions in *MUC16* were similarly observed in both tumor and organoids. *MUC16* encodes for cancer antigen 125 (CA-125), which is not detectable in normal OSE and is therefore used as a biomarker during advanced-stage OC follow-up (Thériault et al., 2011), although its significance remains highly controversial (Stewart et al., 2012). Moreover, we found that nuclear atypia, protein marker expression, and SCNA and mutational profile of the tumors was highly conserved in the corresponding organoids although occasional deviations were observed, which may be due to presence of non-tumor cells in the DNA-extracted primary tissue and/or the selection and growth of (a) specific mutant subclone(s) in the culture conditions used (as also reported for other cancer types; Boretto et al., 2019; Broutier et al., 2017; Van De Wetering et al., 2015). Subclone selection might also match what is happening in the patient's cancer at recurrences during consecutive therapies (e.g., selection of the more dominant or chemoresistant subclone[s]). On the other hand, new mutations arising in the organoids might mimic the "natural" mutational evolution of the cancer (being propelled by cancer driver genes such as MYC) (Boretto et al., 2019).

We found that organoids can also be established from EOC tumor cells remaining after chemotherapy. Chemoresistant cells may represent cancer stem cells postulated to drive OC resistance and recurrence (Garson and Vanderhyden, 2015). The (cancer) stem cell markers *ALDH1A1* and *LGR5* were found to be expressed in some of the organoid lines analyzed. Of note, OSE and FTE contain cells expressing LGR5, which has been suggested to contribute to EOC development (Ng et al., 2014).

Finally, we demonstrated that the EOC-derived organoids are amenable to drug screening and show differential sensitivity of individual patient organoid lines to the chemotherapeutic agents tested. Hence, by predicting patients' tumor responses to specific drugs using the organoids as "avatars," the optimal treatment for the individual patient may be selected (as recently reported for other cancer types; Broutier et al., 2017; Huang et al., 2015; Sachs et al., 2018; Van De Wetering et al., 2015). Moreover, the EOC organoid models will be highly instrumental in moving into the field of immunotherapy (e.g., using CAR-T and natural killer cells), as has recently been shown for colorectal cancer organoids (Schnalzger et al., 2019). Since organoids are typically composed of the epithelial compartment of the original tissue, further perfecting the model by adding stromal and immune components of the tumor microenvironment will eventually be needed to reach the organoid model's full potential.

In summary, we established organoid lines from patient-derived EOC that capture disease and patients' tumor diversity and hallmarks, thereby adding new lines to the existing EOC organoid repertoire, which is essential for gaining deeper insight into the cancer's etiology, pathogenesis, heterogeneity, and chemoresistance, and for identifying new therapeutic targets and screening new drugs, preferably in a patient-tailored manner (also reviewed in Maru and Hippo, 2019). It should be acknowledged that the EOC organoid derivation protocol still deserves further efforts for improvement. The EOC organoid platform has strong potential as an experimental and preclinical research model, and in particular as impetus to revive NRG1/ERBB research in OC, and may eventually identify response-predictive biomarkers, assist in clinical decision making, and provide personalized therapeutic options, particularly for patients in whom standard clinical routes have been exhausted.

EXPERIMENTAL PROCEDURES

Detailed methods are provided in Supplemental Information.

Establishing Organoid Cultures from Patient-Derived EOC Biopsies

EOC biopsies were obtained from patients following standard primary or interval debulking surgery (Table 1). The study was approved by the Ethical Committee Research UZ/KU Leuven (S60589), and written informed consent was obtained from all participating patients. The freshly obtained or cryopreserved tissue was dissociated using collagenase type IV and mechanical shearing. Cells were plated in 70% growth factor-reduced Matrigel/30% Dulbecco's modified Eagle's medium/F12 and cultured in defined media (Table S1), and organoids were passaged between 2 and 4 weeks after seeding.

Immunohistochemical Analysis

Tissues and organoids were fixed in paraformaldehyde and paraffin-embedded sections subjected to H&E, immunohistochemical, and/or immunofluorescence staining (for antibodies, see Supplemental Information). Microscopy pictures were taken and proportions of immunoreactive cells counted using Fiji software (http://imagej.net/Citing).

Genomic Analysis

For array comparative genomic hybridization (array CGH), genomic DNA from organoids and primary tissues was labeled with Cy5 and hybridized to Cy3-labeled sex-matched reference DNA. Arrays were scanned using an Agilent microarray scanner, followed by calculation of signal intensities using Agilent Feature Extraction software.

Sequencing was performed on whole-exome and low-coverage whole-genome DNA libraries by Illumina's NextSeq and HiSeq4000, respectively (Table S4). Raw sequencing reads were aligned to the human reference genome and copy-number variations were identified using the low-coverage whole-genome sequencing data while variants were identified in the whole-exome data and further filtered and annotated to retain somatic mutations, using in-house developed bioinformatics pipelines. Tumor content and corresponding ploidy was quantified with ASCAT.

Targeted Sanger Sequencing

The targeted PCR-amplified *BRCA1* gene region (for primers, see Table S5) was purified and Sanger sequenced by Eurofins Genomics (Ebersberg, Germany).

Gene Expression Analysis

Organoid RNA was reverse transcribed and subjected to quantitative real-time PCR (qPCR) using gene-specific forward and reverse primers (Table S5). Expression levels were normalized to expression of the housekeeping gene glyceraldehyde-3-phosphate dehydrogenase (*GAPDH*). Relative gene expression levels were calculated as ΔC_t values (C_t "target gene" minus C_t "*GAPDH*"), and the corresponding heatmap was generated by Heatmapper (http://www2.heatmapper.ca/expression/).

Drug Screening

Organoid cultures were treated with a concentration series of paclitaxel, carboplatin, doxorubicin, gemcitabine, or nutlin-3. Cell viability was assayed after 72 h using the XTT assay, and data analysis was performed with GraphPad Prism.

Statistical Analyses

Statistical analyses were performed using GraphPad Prism and are specified in the figure legends. Statistical significance was defined as $p < 0.05$. All experiments were performed with ≥ 3 biological replicates unless otherwise indicated.

SUPPLEMENTAL INFORMATION

Supplemental Information can be found online at https://doi.org/10.1016/j.stemcr.2020.03.004.

AUTHOR CONTRIBUTIONS

N.M. designed the concepts and experiments, performed the experiments and the data analysis, interpreted the results, and co-wrote the manuscript; C.D. designed and performed the experiments, executed the data analysis, and interpreted the results; M.B. contributed to the organoid protocol setup and drug screenings; Z.J. collected patients' information and samples and helped in concepts, interpretation of the results, and statistical analyses; R.H. collected patients' information and samples, helped in concepts and interpretation of the results and in maintenance of the organoid cultures; B.B. performed and interpreted the genomic sequencing; F.H. performed a number of gene and protein expression analyses and added conceptual input; I.A. organized and interpreted the genomic sequencing; B.C. added technical and conceptual input; E.V.N. was a collaborating surgeon providing clinical samples; I.V. was a collaborating surgeon providing clinical samples; A-S.V.R. was the pathologist providing expert interpretation of the tumor and organoid histology; D.L. supervised and co-interpreted the genomic sequencing; D.T. was a driving force behind the clinical collaboration to obtain human samples and is a collaborating gynecologist with joint research grants; H.V. designed and supervised the project, co-developed the concepts and ideas, co-designed the experiments, co-analyzed and co-interpreted the data, and wrote the manuscript. All authors critically read and approved the manuscript.

ACKNOWLEDGMENTS

We thank the UZ/KU Leuven Genomics Core for their expert assistance in array CGH analysis, and Thomas Van Brussel (D.L.'s group) for technical help in genome sequencing. We are grateful to Lara Vankelecom (University of Ghent, Faculty of Psychology and Educational Sciences, Department of Data Analysis) for expert help with statistical analyses. The computational resources and services used for genome sequencing and analysis were provided by the Flemish Supercomputer Center (VSC), funded by the Hercules Foundation and the Flemish Government, Department of Economy, Science and Innovation (EWI). We are also grateful to InfraMouse (VIB-KU Leuven, Hercules type 3 project ZW09-03) for use of histological instruments and microscopes. This work was supported by grants from the KU Leuven Research Fund and from the Fund for Scientific Research (FWO) - Flanders (Belgium). N.M. is, and B.C. was, a PhD Fellow of the FWO. D.T. is a Senior Clinical Investigator of the FWO.

Received: July 15, 2019
Revised: March 3, 2020
Accepted: March 3, 2020
Published: April 2, 2020

REFERENCES

Antoniou, A., Pharoah, P.D.P., Narod, S., Risch, H.A., Eyfjord, J.E., Hopper, J.L., Loman, N., Olsson, H., Johannsson, O., Borg, Å., et al. (2003). Average risks of breast and ovarian cancer associated with BRCA1 or BRCA2 mutations detected in case series unselected for family history: a combined analysis of 22 studies. Am. J. Hum. Genet. *72*, 1117–1130.

Aune, G., Lian, A.M., Tingulstad, S., Torp, S.H., Forsmo, S., Reseland, J.E., Stunes, A.K., and Syversen, U. (2011). Increased circulating hepatocyte growth factor (HGF): a marker of epithelial ovarian cancer and an indicator of poor prognosis. Gynecol. Oncol. *121*, 402–406.

Azmi, A.S., Li, Y., Muqbil, I., Aboukameel, A., Senapedis, W., Baloglu, E., Landesman, Y., Shacham, S., Kauffman, M.G., Philip, P.A., et al. (2017). Exportin 1 (XPO1) inhibition leads to restoration of tumor suppressor miR-145 and consequent suppression of pancreatic cancer cell proliferation and migration. Oncotarget *8*, 82144–82155.

Boretto, M., Cox, B., Noben, M., Hendriks, N., Fassbender, A., Roose, H., Amant, F., Timmerman, D., Tomassetti, C., Vanhie, A., et al. (2017). Development of organoids from mouse and human endometrium showing endometrial epithelium physiology and long-term expandability. Development *144*, 1775–1786.

Boretto, M., Maenhoudt, N., Luo, X., Hennes, A., Boeckx, B.B., Bui, B., Heremans, R., Perneel, L., Kobayashi, H., Van Zundert, I., et al. (2019). Patient-derived organoids from endometrial disease capture clinical heterogeneity and are amenable to drug screening. Nat. Cell Biol. *21*, 1041–1051.

Broutier, L., Mastrogiovanni, G., Verstegen, M.M., Francies, H.E., Gavarró, L.M., Bradshaw, C.R., Allen, G.E., Arnes-Benito, R., Sidorova, O., Gaspersz, M.P., et al. (2017). Human primary liver cancer-derived organoid cultures for disease modeling and drug screening. Nat. Med. *23*, 1424–1435.

Camblin, A.J., Tan, G., Curley, M.D., Yannatos, I., Iadevaia, S., Rimkunas, V., Mino-Kenudson, M., Bloom, T., Schoeberl, B., Drummond, D.C., et al. (2019). Dual targeting of IGF-1R and ErbB3 as a potential therapeutic regimen for ovarian cancer. Sci. Rep. *9*, 1–10.

Cathro, H.P., and Stoler, M.H. (2002). Expression of cytokeratins 7 and 20 in ovarian neoplasia. Am. J. Clin. Pathol. *117*, 944–951.

Clevers, H. (2016). Modeling development and disease with organoids. Cell *165*, 1586–1597.

Davies, S., Holmes, A., Lomo, L., Steinkamp, M.P., Kang, H., Muller, C.Y., and Wilson, B.S. (2014). High incidence of ErbB3, ErbB4, and MET expression in ovarian cancer. Int. J. Gynecol. Pathol. *33*, 402–410.

Van De Wetering, M., Francies, H.E., Francis, J.M., Bounova, G., Iorio, F., Pronk, A., Van Houdt, W., Van Gorp, J., Taylor-Weiner, A., Kester, L., et al. (2015). Prospective derivation of a living organoid biobank of colorectal cancer patients. Cell *161*, 933–945.

Drilon, A., Somwar, R., Mangatt, B.P., Edgren, H., Desmeules, P., Ruusulehto, A., Smith, R.S., Delasos, L., Vojnic, M., Plodkowski, A.J., et al. (2018). Response to ERBB3-directed targeted therapy in NRG1-rearranged cancers. Cancer Discov. *8*, 686–695.

Gao, J., Aksoy, B.A., Dogrusoz, U., Dresdner, G., Gross, B., Sumer, S.O., Sun, Y., Jacobsen, A., Sinha, R., Larsson, E., et al. (2013). Integrative analysis of complex cancer genomics and clinical profiles using the cBioPortal. Sci. Signal. *6*, 1–20.

Gao, D., Vela, I., Sboner, A., Iaquinta, P.J., Wouter, R., Arora, V.K., Wongvipat, J., Kossai, M., Ramazanoglu, S., Luendreo, P., et al. (2014). Organoid cultures derived from patients with advanced prostate cancer. Cell *159*, 176–187.

Garson, K., and Vanderhyden, B.C. (2015). Epithelial ovarian cancer stem cells: underlying complexity of a simple paradigm. Reproduction *149*, R59–R70.

Gilmour, L.M.R., Macleod, K.G., Mccaig, A., Sewell, J.M., Gullick, W.J., Smyth, J.F., and Langdon, S.P. (2002). Neuregulin expression, function and signaling in human ovarian cancer cells. Clin. Cancer Res. *8*, 3933–3942.

Hardy, L.R., Salvi, A., and Burdette, J.E. (2018). Unpaxing the divergent roles of PAX2 and PAX8 in high-grade serous ovarian cancer. Cancers (Basel) *10*, 262.

Harris, F.R., Zhang, P., Yang, L., Hou, X., Leventakos, K., Weroha, S.J., Vasmatzis, G., and Kovtun, I.V. (2019). Targeting HER2 in patient-derived xenograft ovarian cancer models sensitizes tumors to chemotherapy. Mol. Oncol. *13*, 132–152.

Hill, S.J., Decker, B., Roberts, E.A., Horowitz, N.S., Muto, M.G., Worley, M.J., Feltmate, C.M., Nucci, M.R., Swisher, E.M., Nguyen, H., et al. (2018). Prediction of DNA repair inhibitor response in short-term patient-derived ovarian cancer organoids. Cancer Discov. *8*, 1404–1421.

Huang, L., Holtzinger, A., Jagan, I., Begora, M., Lohse, I., Ngai, N., Nostro, C., Wang, R., Muthuswamy, L.B., Crawford, H.C., et al. (2015). Ductal pancreatic cancer modeling and drug screening using human pluripotent stem cell- and patient-derived tumor organoids. Nat. Med. *21*, 1364–1371.

Hwang, J.R., Jo, K., Lee, Y., Sung, B.J., Park, Y.W., and Lee, J.H. (2012). Upregulation of CD9 in ovarian cancer is related to the induction of TNF-α gene expression and constitutive NF-κB activation. Carcinogenesis *33*, 77–83.

Jelovac, D., and Armstrong, D.K.D. (2011). Recent progress in the diagnosis and treatment of ovarian cancer. CA Cancer J. Clin. *61*, 183–203.

Kessler, M., Hoffmann, K., Brinkmann, V., Thieck, O., Jackisch, S., Toelle, B., Berger, H., Mollenkopf, H.-J., Mangler, M., Sehouli, J., et al. (2015). The Notch and Wnt pathways regulate stemness and differentiation in human fallopian tube organoids. Nat. Commun. *6*, 8989.

Kim, J., Park, E.Y., Kim, O., Schilder, J.M., Coffey, D.M., Cho, C.H., and Bast, R.C. (2018). Cell origins of high-grade serous ovarian cancer. Cancers (Basel) *10*, 1–28.

Kopper, O., de Witte, C.J., Lõhmussaar, K., Valle-Inclan, J.E., Hami, N., Kester, L., Balgobind, A.V., Korving, J., Proost, N., Begthel, H., et al. (2019). An organoid platform for ovarian cancer captures intra- and interpatient heterogeneity. Nat. Med. *25*, 838–849.

Kuo, K.T., Guan, B., Feng, Y., Mao, T.L., Chen, X., Jinawath, N., Wang, Y., Kurman, R.J., Shih, I.M., and Wang, T.L. (2009). Analysis of DNA copy number alterations in ovarian serous tumors identifies new molecular genetic changes in low-grade and high-grade carcinomas. Cancer Res. *69*, 4036–4042.

Lazennec, G. (2006). Estrogen receptor beta, a possible tumor suppressor involved in ovarian carcinogenesis. Cancer Lett. *231*, 151–157.

Lengyel, E., Burdette, J., Kenny, H., Matei, D., Pilrose, J., Haluska, P., Nephew, K., Hales, D., and Stack, M. (2014). Epithelial ovarian cancer experimental models. Oncogene *33*, 3619–3633.

Luo, H., Xu, X., Ye, M., Sheng, B., and Zhu, X. (2018). The prognostic value of HER2 in ovarian cancer: a meta-analysis of observational studies. PLoS One *13*, 1–16.

Maru, Y., and Hippo, Y. (2019). Current status of patient-derived ovarian cancer models. Cells *8*, 505.

Maru, Y., Tanaka, N., Itami, M., and Hippo, Y. (2019). Efficient use of patient-derived organoids as a preclinical model for gynecologic tumors. Gynecol. Oncol. *154*, 189–198.

Narod, S. (2016). Can advanced-stage ovarian cancer be cured? Nat. Rev. Clin. Oncol. *13*, 255–261.

Ng, A., Tan, S., Singh, G., Rizk, P., Swathi, Y., Tan, T.Z., Huang, R.Y.J., Leushacke, M., and Barker, N. (2014). Lgr5 marks stem/progenitor cells in ovary and tubal epithelia. Nat. Cell Biol. *16*, 745–757.

Ocana, A., Vera-Badillo, F., Seruga, B., Templeton, A., Pandiella, A., and Amir, E. (2013). HER3 overexpression and survival in solid tumors: a meta-analysis. J. Natl. Cancer Inst. *105*, 266–273.

Pennington, K.P., Walsh, T., Harrell, M.I., Lee, M.K., Pennil, C.C., Rendi, M.H., Thornton, A., Norquist, B.M., Casadei, S., Nord, A.S., et al. (2014). Germline and somatic mutations in homologous recombination genes predict platinum response and survival in ovarian, fallopian tube, and peritoneal carcinomas. Clin. Cancer Res. *20*, 764–775.

Pignata, S., Cecere, S.C., Du Bois, A., Harter, P., and Heitz, F. (2017). Treatment of recurrent ovarian cancer. Ann. Oncol. *28*, viii51–viii56.

Rajkumar, T., Stamp, G.W.H., Hughes, C.M., and Gullick, W.J. (1996). c-erbB3 protein expression in ovarian cancer. Clin. Mol. Pathol. *49*, 1–4.

Sachs, N., and Clevers, H. (2014). Organoid cultures for the analysis of cancer phenotypes. Curr. Opin. Genet. Dev. *24*, 68–73.

Sachs, N., de Ligt, J., Kopper, O., Gogola, E., Bounova, G., Weeber, F., Balgobind, A.V., Wind, K., Gracanin, A., Begthel, H., et al. (2018). A living biobank of breast cancer organoids captures disease heterogeneity. Cell *172*, 373–386.e10.

Schnalzger, T.E., de Groot, M.H., Zhang, C., Mosa, M.H., Michels, B.E., Röder, J., Darvishi, T., Wels, W.S., and Farin, H.F. (2019). 3D model for CAR-mediated cytotoxicity using patient-derived colorectal cancer organoids. EMBO J. *38*, e100928.

Schummer, M., Ng, W.V., Bumgarner, R.E., Nelson, P.S., Schummer, B., Bednarski, D.W., Hassell, L., Baldwin, R.L., Karlan, B.Y., and Hood, L. (1999). Comparative hybridization of an array of 21 500 ovarian cDNAs for the discovery of genes overexpressed in ovarian carcinomas. Gene *238*, 375–385.

Serrano-Olvera, A., Dueñas-González, A., Gallardo-Rincón, D., Candelaria, M., and De la Garza-Salazar, J. (2006). Prognostic, predictive and therapeutic implications of HER2 in invasive epithelial ovarian cancer. Cancer Treat. Rev. *32*, 180–190.

Sheng, Q., Liu, X., Fleming, E., Yuan, K., Piao, H., Chen, J., Moustafa, Z., Thomas, R.K., Greulich, H., Schinzel, A., et al. (2010). An activated ErbB3/NRG1 autocrine loop supports in vivo proliferation in ovarian cancer cells. Cancer Cell *17*, 298–310.

Shu, T., Li, Y., Wu, X., Li, B., and Liu, Z. (2017). Down-regulation of HECTD3 by HER2 inhibition makes serous ovarian cancer cells sensitive to platinum treatment. Cancer Lett. *411*, 65–73.

Sondka, Z., Bamford, S., Cole, C.G., Ward, S.A., Dunham, I., and Forbes, S.A. (2018). The COSMIC Cancer Gene Census: describing genetic dysfunction across all human cancers. Nat. Rev. Cancer *18*, 696–705.

Stewart, S.L., Rim, S.H., and Gelb, C.A. (2012). Physician knowledge and awareness of CA-125 as a screen for ovarian cancer in the asymptomatic, average-risk population. Heal. Educ. Behav. *39*, 57–66.

The Cancer Genome Atlas Research Network (2011). Integrated genomic analyses of ovarian carcinoma. Nature *474*, 609–615.

Thériault, C., Pinard, M., Comamala, M., Migneault, M., Beaudin, J., Matte, I., Boivin, M., Piché, A., and Rancourt, C. (2011). MUC16 (CA125) regulates epithelial ovarian cancer cell growth, tumorigenesis and metastasis. Gynecol. Oncol. *121*, 434–443.

Timmermans, M., Sonke, G.S., Van de Vijver, K.K., van der Aa, M.A., and Kruitwagen, R.F.P.M. (2018). No improvement in long-term survival for epithelial ovarian cancer patients: a population-based study between 1989 and 2014 in The Netherlands. Eur. J. Cancer *88*, 31–37.

Toss, A., Tomasello, C., Razzaboni, E., Contu, G., Grandi, G., Cagnacci, A., Schilder, R.J., and Cortesi, L. (2015). Hereditary ovarian cancer: not only BRCA 1 and 2 genes. Biomed. Res. Int. *2015*, 341723.

Voutsadakis, I.A. (2016). Hormone receptors in serous ovarian carcinoma: prognosis, pathogenesis, and treatment considerations. Clin. Med. Insights Oncol. *10*, 17–25.

Walsh, A.J., Cook, R.S., Sanders, M.E., Arteaga, C.L., and Skala, M.C. (2016). Drug response in organoids generated from frozen primary tumor tissues. Sci. Rep. *6*. https://doi.org/10.1038/srep18889.

Wang, M., Ma, H., Pan, Y., Xiao, W., Li, J., Yu, J., and He, J. (2015). PAX2 and PAX8 reliably distinguishes ovarian serous tumors from mucinous tumors. Appl. Immunohistochem. Mol. Morphol. *23*, 280–287.

Wang, S., Cheng, Y., Zheng, Y., He, Z., Chen, W., Zhou, W., Duan, C., and Zhang, C. (2016). PRKAR1A is a functional tumor suppressor inhibiting ERK/Snail/E-cadherin pathway in lung adenocarcinoma. Sci. Rep. *6*, 1–12.

Xie, L., Ushmorov, A., Leithäuser, F., Guan, H., Steidl, C., Färbinger, J., Pelzer, C., Vogel, M.J., Maier, H.J., Gascoyne, R.D., et al. (2012). FOXO1 is a tumor suppressor in classical Hodgkin lymphoma. Blood *119*, 3503–3511.

Yan, H.H.N., Siu, H.C., Law, S., Ho, S.L., Yue, S.S.K., Tsui, W.Y., Chan, D., Chan, A.S., Ma, S., Lam, K.O., et al. (2018). A comprehensive human gastric cancer organoid biobank captures tumor subtype heterogeneity and enables therapeutic screening. Cell Stem Cell *23*, 882–897.e11.

Zanjirband, M., Curtin, N., Edmondson, R.J., and Lunec, J. (2017). Combination treatment with rucaparib (Rubraca) and MDM2 inhibitors, Nutlin-3 and RG7388, has synergistic and dose reduction potential in ovarian cancer. Oncotarget *8*, 69779–69796.

Zhang, J., Vlasevska, S., Wells, V.A., Nataraj, S., Holmes, A.B., Duval, R., Meyer, S.N., Mo, T., Basso, K., Brindle, P.K., et al. (2017). The CREBBP acetyltransferase is a haploinsufficient tumor suppressor in B-cell lymphoma. Cancer Discov. *7*, 323–337.

Stem Cell Reports, Volume *14*

Supplemental Information

Developing Organoids from Ovarian Cancer as Experimental and Pre-clinical Models

Nina Maenhoudt, Charlotte Defraye, Matteo Boretto, Ziga Jan, Ruben Heremans, Bram Boeckx, Florian Hermans, Ingrid Arijs, Benoit Cox, Els Van Nieuwenhuysen, Ignace Vergote, Anne-Sophie Van Rompuy, Diether Lambrechts, Dirk Timmerman, and Hugo Vankelecom

SUPPLEMENTAL FIGURES AND LEGENDS

Figure S1

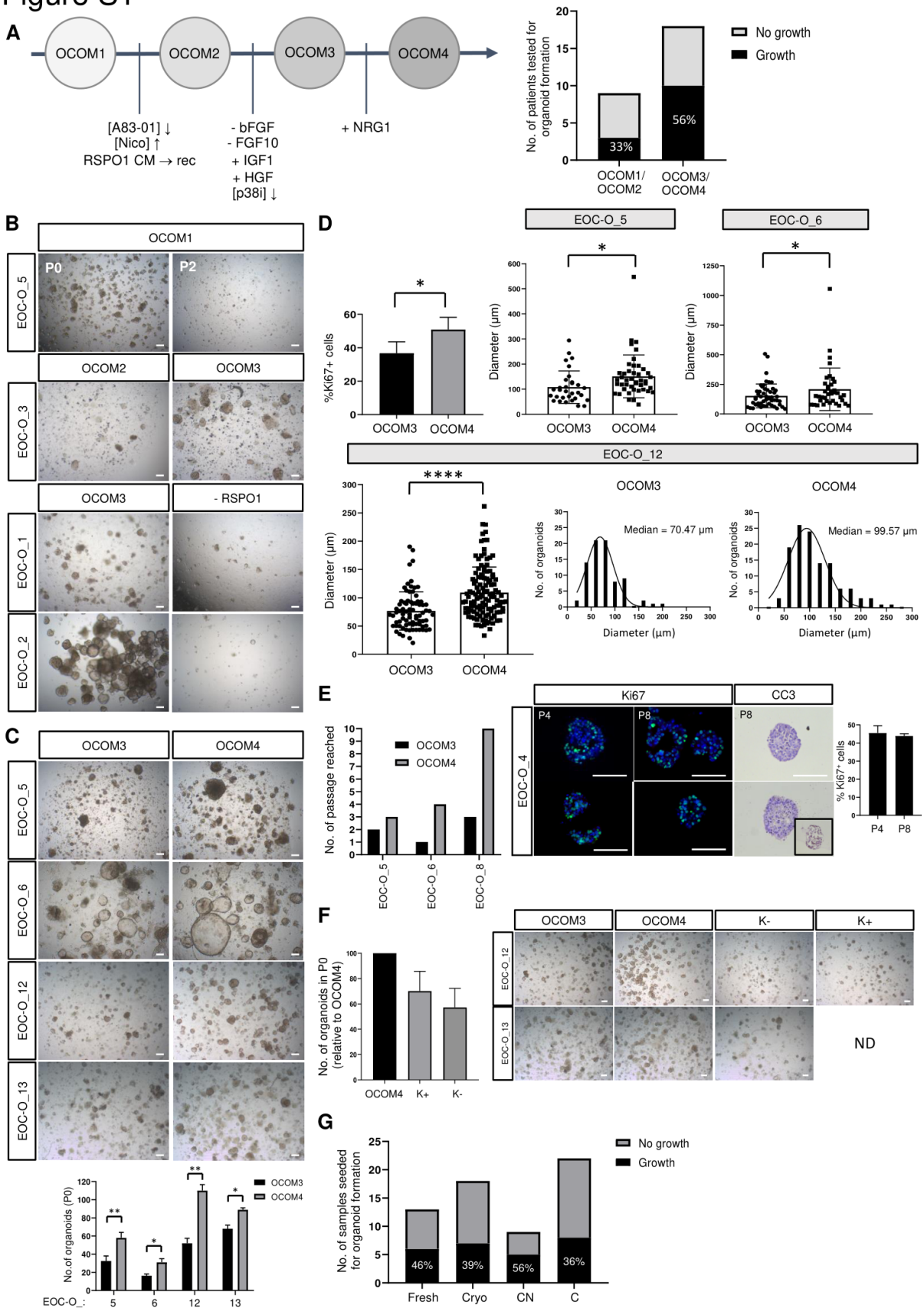

Figure S1. EOC organoid culture optimization

(A) Flow chart of the culture medium optimization process with medium composition changes as indicated (left) and organoid formation efficiency (right; total number of patients tested per medium group with indication of the proportion of patients which initiated organoid growth). OCOM, ovarian cancer organoid medium; Nico, nicotinamide; CM, conditioned medium; rec, recombinant; P, passage.

(B) Representative examples (brightfield pictures) of the limited organoid passageability in OCOM1, and of the beneficial effect of lowering p38i (from OCOM2 to OCOM3), and of the essential presence of RSPO1 in organoid formation (P0) are shown. Scale bars, 200 µm.

(C) Positive impact of NRG1 on EOC organoid development and growth. Representative brightfield images of several organoid lines in OCOM3 and OCOM4 are shown. Scale bars, 200 µm. Bar graphs display the number of organoids formed in P0 (mean ± SEM, n=3 independent experiments; *p < 0.05, **p < 0.01; Student's t-test).

(D) Positive impact of NRG1 on proliferative activity and size of EOC organoids. Bars display the proportion of $Ki67^+$ cells (left; mean ± SEM, n=3 independent experiments; *p < 0.05; Student's t-test) and the diameters (showing individual organoid data points) of 3 independent organoid lines (P0) in OCOM3 and OCOM4, together with the size distribution histogram as representative example for EOC-O_12 (mean ± SD; *p < 0.05, ****p < 0.001; Student's t-test).

(E) Long-term expansion of EOC organoids. Bar graph presents the (at present maximum) passage number reached in the indicated organoid lines in OCOM3 and OCOM4. Representative images of Ki67 and CC3 immunostaining analysis at later passages (P4 and P8, meaning 4 and 10 months of propagation, respectively) are displayed (DAPI and hematoxylin as nuclear stains). Inset shows a positive control for CC3 immunostaining (i.e. apoptotic organoid after chemotherapy). Bar graph depicts the proportion of $Ki67^+$ cells in the passages as indicated (mean ± SD of triplicate analyses). Scale bars, 200 µm.

(F) Comparable organoid initiation (P0) in OCOM4 and 'Kopper' (K) medium, with (+) or without (-) WNT3A. Bar graph shows organoid formation efficiency (number of organoids formed relative to

OCOM4, set as 100 %) (mean ± SEM, n=4 independent experiments). Differences between culture media are non-significant (Student's t-test; $p > 0.05$). Representative brightfield images are shown in the different culture conditions (right). Scale bars, 200 µm.

(G) Organoid formation efficiency from freshly obtained and cryopreserved EOC biopsies, and from samples of patients with or without prior chemotherapy. Bars show the total number of EOC samples seeded per group with indication of the proportion of samples that initiated organoid growth. Differences between fresh and cryo, and between chemo-naive (CN) and chemotherapy-treated (C) are non-significant (Fisher's exact test on contingency tables; $p > 0.05$).

Figure S2

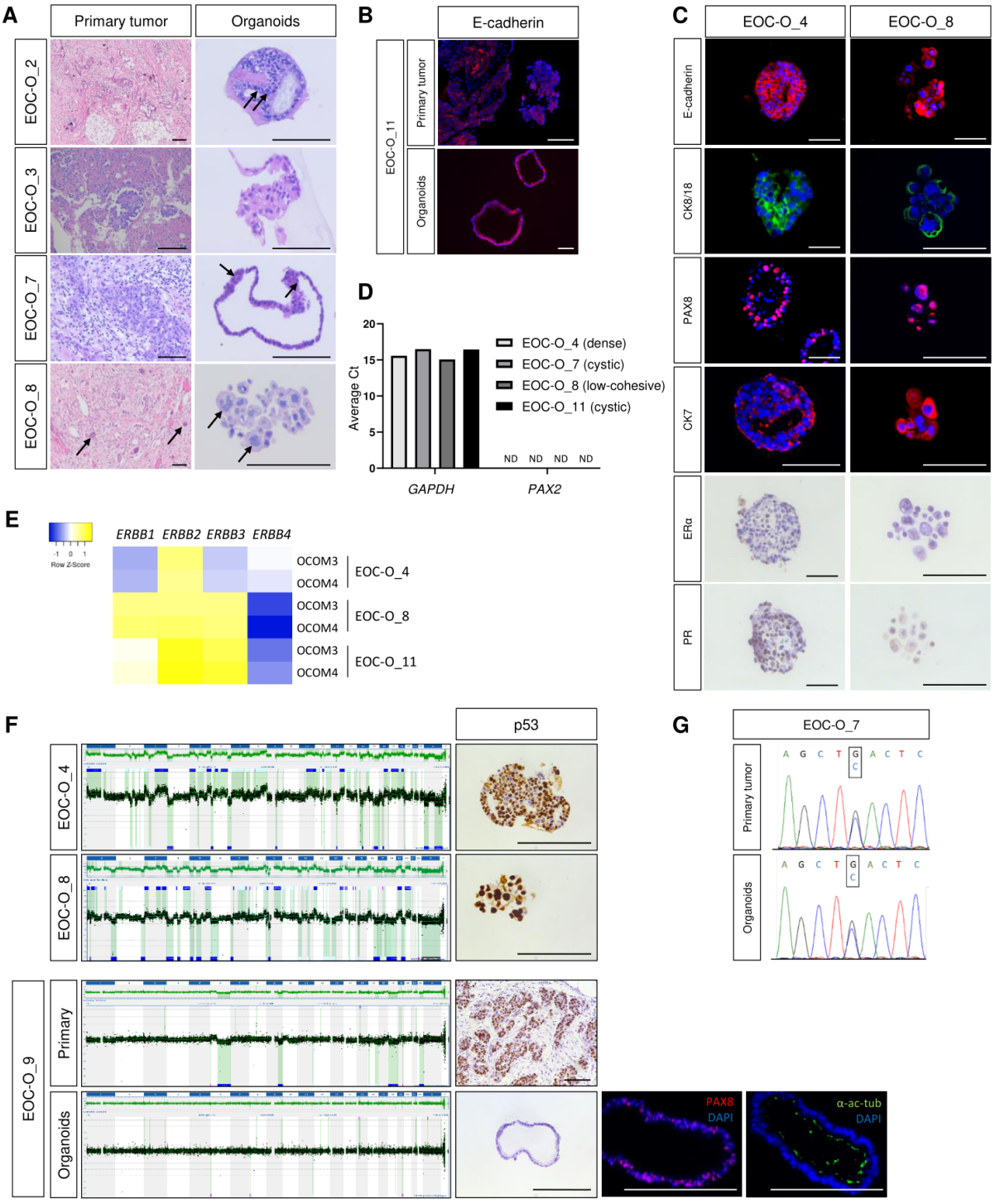
A
Primary tumor
Organoids
EOC-O_2
EOC-O_3
EOC-O_7
EOC-O_8
B
E-cadherin
EOC-O_11
Primary tumor
Organoids
C
EOC-O_4
EOC-O_8
E-cadherin
CK8/18
PAX8
CK7
ERα
PR
D
Average Ct
20
15
10
5
0
EOC-O_4 (dense)
EOC-O_7 (cystic)
EOC-O_8 (low-cohesive)
EOC-O_11 (cystic)
ND ND ND ND
GAPDH
PAX2
E
ERBB1 ERBB2 ERBB3 ERBB4
Row Z-Score
OCOM3
OCOM4
EOC-O_4
EOC-O_8
EOC-O_11
F
p53
EOC-O_4
EOC-O_8
EOC-O_9
Primary
Organoids
PAX8
DAPI
α-ac-tub
DAPI
G
EOC-O_7
Primary tumor
Organoids

Figure S2. EOC-derived organoids capture disease and primary tumor phenotype

(A) Organoids show nuclear atypia as present in the original tumor. Representative pictures of H&E staining in primary tumor and organoids are shown. The primary tissue of EOC-O_2 and EOC-O_7 shows abundant nuclear atypia which are also found in the organoids (some indicated with arrows). EOC-O_3 represents a LGSOC (Table 1), known to contain less atypia. In EOC-O_8, multinucleated giant cells are found in primary tissue and are also present in the organoids (some indicated by arrows). Scale bars, 200 μm.

(B) Organoids show epithelial marker expression as present in the tumor (epithelial) cells. Representative pictures of immunofluorescence analysis of E-cadherin are shown (DAPI as nuclear stain). Scale bars, 200 μm.

(C) Organoids show EOC-associated protein marker expression. Representative pictures of immunostaining analyses are shown (DAPI or hematoxylin as nuclear stain). CK, cytokeratin; ERα, estrogen receptor-α; PR, progesterone receptor. Scale bars, 100 μm.

(D) The organoids do not express *PAX2*, as characteristic for HGSOC. Bars indicate average C_t value of 2 technical replicates, as determined by RT-qPCR for *GAPDH* and *PAX2* in organoids from different patients (with different morphology). ND, not detectable.

(E) *ERBB* expression profile in organoids (P2-P5) grown without NRG1 (OCOM3) or with NRG1 (OCOM4) as quantified by RT-qPCR and presented as relative expression to *GAPDH* (ΔC_t), visualized as color-coded Row Z-score. Colors range from blue (low expression) to yellow (high expression).

(F) Organoids show a genomic landscape in accordance with a HGSOC genotype (i.e. with prominent SCNA). Representative array CGH plots are shown of two EOC-derived organoid lines (ECO-O_4, ECO-O_8; analyzed at P2-P4) (upper left), and corresponding p53 immunostaining of the organoids (upper right), indicating the major tumor cell content.

Absence of SCNA in EOC-O_9 organoids (while present in the primary tissue) indicates culture overtaking by healthy tissue organoids (lower left). The tumor's cellular and $p53^+$ phenotype is also

absent in the organoids (lower right). Immunofluorescence analysis of PAX8 and α-acetylated tubulin (α-ac-tub) supports an FTE phenotype (DAPI as nuclear stain). Scale bars, 200 µm.

(G) Organoids established from the EOC sample of a germline *BRCA1* mutant patient. Sanger sequencing chromatograms show the heterozygote G to C mutation at position 43071154 in the *BRCA1* gene (NC_000017.1, GRCh38; leading to a premature stop codon) in the primary patient tumor (as also reported in the patient dossier) and in the derived organoids (analyzed at P4).

Figure S3

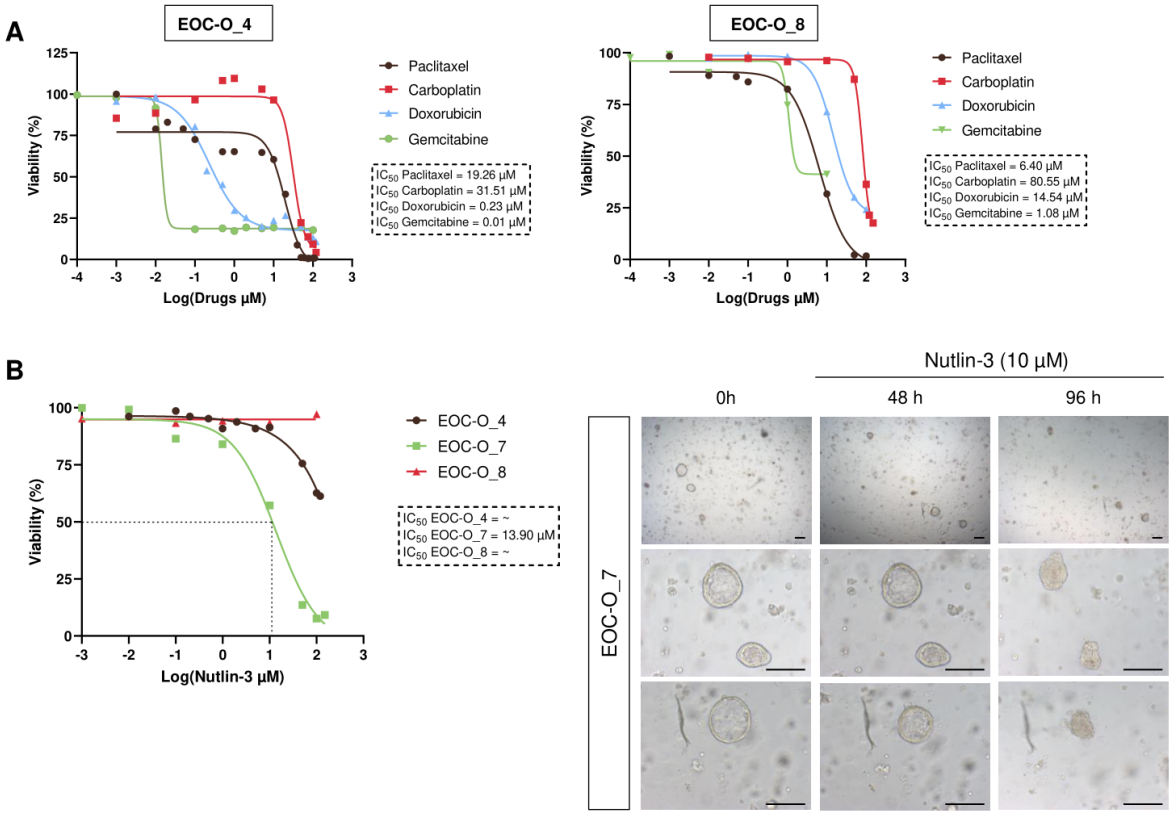
A
EOC-O_4
Viability (%)
Log(Drugs µM)
Paclitaxel
Carboplatin
Doxorubicin
Gemcitabine
IC50 Paclitaxel = 19.26 µM
IC50 Carboplatin = 31.51 µM
IC50 Doxorubicin = 0.23 µM
IC50 Gemcitabine = 0.01 µM
EOC-O_8
Viability (%)
Log(Drugs µM)
Paclitaxel
Carboplatin
Doxorubicin
Gemcitabine
IC50 Paclitaxel = 6.40 µM
IC50 Carboplatin = 80.55 µM
IC50 Doxorubicin = 14.54 µM
IC50 Gemcitabine = 1.08 µM
B
Viability (%)
Log(Nutlin-3 µM)
EOC-O_4
EOC-O_7
EOC-O_8
IC50 EOC-O_4 = ~
IC50 EOC-O_7 = 13.90 µM
IC50 EOC-O_8 = ~
Nutlin-3 (10 µM)
0h
48 h
96 h
EOC-O_7

Figure S3. Individual patient EOC-derived organoids show drug-specific sensitivities

(A) Dose-response curves of different chemotherapeutic drugs in 2 individual EOC organoid lines are shown. Cell viability was measured after 72h drug treatment using XTT assay. Mean data points (n=4 independent drugs and each dot represents the mean of 3 technical replicates per drug) are displayed for each concentration analyzed.

(B) Dose-response curves (left) of EOC organoid cultures from different patients treated for 72h with nutlin-3 are shown. Cell viability was measured using XTT assay. Mean data points (n=3 biologically independent experiments, i.e. independent donors, and each dot represents the mean of 3 technical replicates per donor) are displayed for each concentration analyzed. IC_{50} values are determined (dashed lines) and indicated. IC_{50} value for EOC-O_4 is 247133 µM, indicating that the sample is nutlin-3-resistant. Brightfield pictures (right) of EOC-O_7 cultures (at P7; overview and individual organoids) treated with nutlin-3 for the indicated period of time. Scale bars, 200 µm.

SUPPLEMENTAL TABLES

Table S1. Ovarian cancer organoid medium (OCOM) compositions

Product	OCOM1	OCOM2	OCOM3	OCOM4	Supplier	Kopper et al. (2019)
DMEM/F12					Thermo Fisher Scientific	
L-glutamine	1X	1X	1X	1X	Thermo Fisher Scientific	/
Pen/Strep	1X	1X	1X	1X	Sigma-Aldrich	0.2% (Primocin)
A83-01	0.5 µM	0.25 µM	0.25 µM	0.25 µM	Sigma-Aldrich	0.5 µM
Nicotinamide	1 mM	5 mM	5 mM	5 mM	Sigma-Aldrich	10 mM
N2	1X	1X	1X	1X	Thermo Fisher Scientific	/
B27 minus vitamin A	1X	1X	1X	1X	Thermo Fisher Scientific	1X
N-acetylcysteine	1.25 mM	1.25 mM	1.25 mM	1.25 mM	Thermo Fisher Scientific	1.25 mM
17-β Estradiol	10 nM	10 nM	10 nM	10 nM	Sigma-Aldrich	100 nM
p38i (SB203580)	10 µM	10 µM	1 µM	1 µM	Sigma-Aldrich	/
EGF	50 ng/ml	50 ng/ml	50 ng/ml	50 ng/ml	R&D systems	5 ng/ml
bFGF	2 ng/ml	2 ng/ml	/	/	R&D systems	/
FGF10	10 ng/ml	10 ng/ml	/	/	Peprotech	10 ng/mL
Noggin (rec or CM)[a]	10% or 100 ng/mL	100 ng/mL	100 ng/mL	100 ng/mL	Homemade or R&D systems	1%
RSPO1 (rec or CM)	25%	50 ng/mL	50 ng/mL	50 ng/mL	Homemade or Peprotech	10%
IGF1	/	/	20 ng/mL	20 ng/mL	Peprotech	/
HGF	/	/	10 ng/mL	10 ng/mL	Peprotech	/
NRG1	/	/	/	50 ng/mL	Peprotech	37.5 ng/ml
WNT3A	/	/	/	/		20% CM[b]
Forskolin	/	/	/	/		10 µM
Hydrocortisone	/	/	/	/		500 ng/mL
Y27632	10 µM[c]	10 µM[c]	10 µM[c]	10 µM[c]	Merck Millipore	5 µM

[a]rec, recombinant; CM, conditioned medium

[b]Depending on patient tumor (Kopper et al. 2019)

[c]Only for organoid initiation and for passaging immediately after dissociation

Table S2. Organoid derivation efficiency and comparison with Kopper et al. (2019)

Overall efficiency

All OC types	Total # of patients	# of patients showing organoid growth	Derivation efficiency
Present study	27	12[a]	44%
Kopper et al. (2019) (Suppl. Table 4)	49	32	65%
HGSOC[b]			
Present study	22	8[a]	36%
Kopper et al. 2019 (Suppl. Table 4)	29	16	55%

[a]Patient 21 (see Table 1) is not included since the organoid line (EOC-O_9) turned out to be non-tumor (healthy).
[b]Comparison regarding subtypes is only meaningful for HGSOC as predominantly analyzed in our study.

Long-term culture efficiency

HGSOC[a]	Total # of organoid lines developed	# of long-term culture organoid lines	Efficiency
Present study	8[b]	5[b]	63%
Kopper et al. (2019) (Suppl. Table 3, Extended Data Fig. 2A)	23	14	61%

[a]Comparison is only meaningful for HGSOC as predominantly analyzed in our study.
[b]Patient 21 (see Table 1) is not included since the organoid line (EOC-O_9) turned out to be non-tumor (healthy).

Table S3. Overview of the 1638 genetic alterations

Table S4. Genome sequencing metrics

Whole-exome sequencing (WES)

Sample	Mean target coverage	Fraction covered >10x	Fraction covered >20x
EOC-O_2	83.79	0.92	0.86
EOC-T_2	69.41	0.90	0.82
EOC-O_6	95.87	0.92	0.88
EOC-T_6	99.80	0,92	0.89
EOC-O_11	46.15	0.86	0.70
EOC-T_11	57.01	0.90	0.81
EOC-O_13	79.30	0.91	0.84
EOC-T_13	61.81	0.90	0.79

T: tumor

Low-coverage whole-genome sequencing

Sample	mapped
EOC-O_7_O1	10319735
EOC-O_7_O2	11349583
EOC-T_7	7803813
EOC-O_12_O1	9733675
EOC-O_12_O2	10464180
EOC-T_12	8595522
EOC-O_2	8918844
EOC-T_2	9425695
EOC-O_11	7230768
EOC-T_11	6133741
EOC-O_6	46019661
EOC-T_6	48816522
EOC-O_13	8355771
EOC-T_13	7631691

T: tumor

Table S5. Primers

Primers used for qPCR

Gene symbol	Gene name	Forward primer	Reverse primer
ALDH1A1	Aldehyde Dehydrogenase 1 Family Member A1	ccgtggcgtactatggatgc	gcagcagacgatctctttcgat
AURA	Aurora kinase A	gctggagagcttaaaattgca	ttttgtaggtctcttggtatgtg
CCND1	Cyclin D1	tctacaccgacaactccatccg	tctggcattttggagaggaagtg
CCNE1	Cyclin E1	tgtgtcctggatgttgactgcc	ctctatgtcgcaccactgatacc
CD9	Antigen CD9	tcgccattgaaatagctgcggc	cgcatagtggatggctttcagc
CK17	Cytokeratin 17	atcctgctggatgtgaagacgc	tccacaatggtacgcacctgac
CK19	Cytokeratin 19	agctagaggtgaagatccgcga	gcaggacaatcctggagttctc
CK20	Cytokeratin 20	atcaagcagtggtacgaa	aggacacaccgagcattt
CK7	Cytokeratin 7	gggctcctgaaggcttattc	gggtgggaatcttcttgtga
CK8	Cytokeratin 8	cgaggatattgccaaccgcag	cctcaatctcagcctggagcc
CLDN3	Claudin 3	aacaccattatccgggacttct	gcggagtagacgaccttgg
C-MYC	MYC Proto-Oncogene	tgaggagacaccgcccac	caacatcgatttcttcctcatcttc
E2F1	E2F Transcription Factor 1	ggacctggaaactgaccatcag	cagtgaggtctcatagcgtgac
E2F3	E2F Transcription Factor 3	agcggtcatcagtacctctcag	tggtgagcagaccaagagacgt
ERα	Oestrogen receptor α	gaaaggtgggatacgaaaagacc	gctgttcttcttagagcgtttga
ERβ	Oestrogen receptor β	atggagtctggtcgtgtgaagg	taacacttccgaagtcggcagg
ERBB1 (EGFR)	Erb-b2 receptor tyrosine kinase 1 (epidermal growth factor receptor)	aacaccctggtctggaagtacg	tcgttggacagccttaagacc
ERBB2	Erb-b2 receptor tyrosine kinase 2	ggaagtacacgatgcggagact	accttcctcagctccgtctt
ERBB3	Erb-b2 receptor tyrosine kinase 3	ctatgaggcgatacttggaacgg	gcacagttccaaagacacccga
ERBB4	Erb-b2 receptor tyrosine kinase 4	ggagtatgtccacgagcacaag	cgagtcgtctttcttccaggtac
FOLRα	Folate receptor α	ctggctggtgttggtagaaca	aggccccgaggacaagtt
GAPDH	Glyceraldehyde-3-phosphate dehydrogenase	ggtatcgtggaaggactcatgac	atgccagtgagcttcccgttcag
HE4	Human epididymis secretory protein 4	agaactgcacgcaagagtg	ttgaggttgtcggcgcatt
KLK6	Kallikrein Related Peptidase 6	tggtgctgagtctgattgct	cgccatgcaccaacttatt
KLK7	Kallikrein Related Peptidase 7	aattccatgctgtgcgctg	aaagttccccaggacaccagac
KLK8	Kallikrein Related Peptidase 8	cagcaaaggggctgacac	gacctcccacaggggtct
LGR5	Leucine Rich Repeat Containing G Protein-Coupled Receptor 5	cacctcctacctagacctcagt	cgcaagacgtaactcctccag
MMP2	Matrix metalloproteinase-2	agcgagtggatgccgcctttaa	cattccaggcatctgcgatgag

MUC1	Mucin 1	cctaccatcctatgagcgagtac	gctgggtttgtgtaagagaggc
MUC16	Mucin 16	gatgtcaagccaggcagcacaa	gagagtggtagacatttctgggc
NOTCH1	Neurogenic Locus Notch Homolog Protein 1	tggaccagattggggagttc	gcacactcgtctgtgttgac
NOTCH3	Neurogenic Locus Notch Homolog Protein 3	ctgcaaggaccgagtcaatgg	cgtccacgttgcgatcacac
PAX2	Paired box gene 2	catgtcacgaccagtcacacc	tgcagatagactcgacttgactt
PAX8	Paired box gene 8	atccggcctggagtgatagg	tggcgtttgtagtccccaatc
PIK3CA	Phosphoinositide-3-Kinase Catalytic Alpha Polypeptide	gaagcacctgaataggcaagtcg	gagcatccatgaaatctggtcgc
PTEN	Phosphatase And Tensin Homolog	agggacgaactggtgtaatga	ctggtccttacttccccatagaa

Primers used to PCR-amplify *BRCA1* gene region for Sanger sequencing

Primer pair	Forward primer	Reverse primer
1	caccaccatggacattcttttgttg	tttctgttgaagctgtcaattctgg
2	caccaacactgtattcatgtaccc	aagctactttggatttccaccaacac

EXPERIMENTAL PROCEDURES

Establishing organoid cultures from patient-derived EOC biopsies

Epithelial ovarian cancer (EOC) biopsies (~1–3 cm^3) were obtained from the University Hospital Leuven (UZ Leuven) following standard primary or interval debulking surgery (Table 1). The study was approved by the Ethical Committee Research UZ/KU Leuven (ethical dossier S60589, Belgian registration number B322201733317), and written informed consent was obtained from all participating patients. EOC specimens were collected in DMEM/F12 (Thermo Fisher Scientific) supplemented with 10% fetal bovine serum (FBS; Thermo Fisher Scientific) and 2% penicillin/streptomycin (Sigma-Aldrich), and kept on ice. Each tumor biopsy was split into 2-3 parts, i.e. for organoid culture, cryopreservation and/or histological analysis. For cryopreservation, fragmented tissue was resuspended in 60% DMEM/F12, 30% FBS and 10% dimethyl sulfoxide (DMSO; Sigma-Aldrich), stored overnight at -80°C and subsequently moved to liquid nitrogen until further processing. For organoid culture, the tissue part was cut into small pieces and rinsed extensively with Ca^{2+}/Mg^{2+}-free PBS (PBS0; Thermo Fisher Scientific). The tissue was dissociated using collagenase type IV (2 mg/mL; Thermo Fisher Scientific) in DMEM/F12 for 1-2h at 37°C. Every 20 min the tissue was mechanically sheared using a fire-polished Pasteur pipet. The suspension was incubated with DNase (Sigma-Aldrich; 50 µl in 4.5 ml DMEM/F12) for 1 min at room temperature. Enzymatic reactions were stopped by doubling the medium volume with DMEM/F12 supplemented with 10% FBS. In case of remaining cell fragments, the solution was filtered through a 70 µm cell strainer (Corning). After centrifugation at 220g for 5 min (4°C), the pellet was resuspended in 70% growth factor-reduced Matrigel (Corning)/30% DMEM/F12 in the presence of the Rho-associated, coiled-coil containing protein kinase inhibitor (ROCKi) Y-27632 (10 µM; Merck Millipore), and 20 µL drops (containing 30.000 cells) were allowed to solidify on pre-warmed 48-well plates at 37°C/5% CO_2 for 20 min. Subsequently, prewarmed culture medium was added (for composition of the different culture media, see Table S1). Cultures were kept at 37°C in a 5% CO_2 incubator and medium was refreshed every 2–3 days. To bring

cryopreserved tissue in culture, samples were thawed at 37°C and DMEM/F12 supplemented with 10% FBS added. Further digestion and seeding were done as described above.

Organoid passaging was performed between 2 and 4 weeks after seeding, depending on the growth rate of the specific tumor. Organoids were recovered from the Matrigel drop and dissociated in TrypLE Express (Thermo Fisher Scientific), containing ROCKi, at 37°C for 5 min (cystic and low-cohesive organoids) or 10 min (dense organoids). After TrypLE inactivation by 1:1 medium dilution, the suspension was centrifuged at 220 g (5 min, 4°C). Mechanical trituration through intense pipetting generated single cells and cell clumps. After another centrifugation step, cells were re-seeded as described above. Brightfield pictures of organoid cultures were recorded using an Axiovert 40 CFL microscope (Zeiss). Expanding organoid lines were subjected to downstream analyses (see below) and cryopreserved. Cryopreservation of dissociated cells was done as described above. Cryopreserved organoid lines were thawed and reseeded according to the protocol mentioned above, thereby again giving rise to organoid cultures (data not shown).

Immunohistochemical analysis

Tissues and organoids were fixed in paraformaldehyde (PFA, 4% in PBS0) overnight at 4°C and for 1h at room temperature, respectively. Then, tissues and organoids were paraffin-embedded and 5-µm sections were subjected to haematoxylin and eosin (H&E), immunohistochemical and/or immunofluorescence staining. Antibodies used in this study were as follows: estrogen receptor-α (Agilent, IR08461-2; ready-to-use); progesterone receptor (Agilent, IR06861-2; ready-to-use); cytokeratin 7 (Proteintech, 22208-I-AP; 1:50); E-cadherin (Cell signaling technology, 3195; 1:200); PAX8 (Proteintech, 10336-I-AP; 1:100); cytokeratin 8/18 (Progen, GP11; 1:500); Ki67 (Novus Biological, NB500-170; 1:100); p53 (Santa Cruz Biotechnology, SC-126; 1:250) for immunofluorescence; p53 (Dako, GA61661-2; ready-to-use) for immunohistochemistry; cleaved caspase 3 (EMD Millipore, AB3623; 1:100); and acetylated α-tubulin (Sigma-Aldrich, T7451; 1:300). Antigen retrieval was performed with citrate-based buffer (10 mM trisodium-citrate in H2O, pH 6; Merck) for 30 min at 95°C,

permeabilization with PBT (0.1% Triton-X in PBS0) and blocking with 0.15% glycine/2 mg/ml bovine serum albumin (BSA) in PBT (and 10% donkey serum (Sigma-Aldrich) for immunofluorescent staining). Incubation with primary antibodies was done overnight at 4°C. Visualization was achieved with secondary anti-mouse/rabbit IgG antibody (ImmPress HRP reagent peroxidase universal anti-mouse/rabbit IgG; Vector Laboratories) (for 30 min at room temperature) and 3'-diaminobenzidine (DAB HRP substrate; Vector Laboratories), or Alexa Fluor 488-/555-labelled donkey antibodies (Thermo Fisher Scientific; A-21206, A-31572, A-21202, A-31570; 1:1000) and fluorescein (FITC)-labelled donkey antibodies (Jackson ImmunoResearch, 706-095-148; 1:1000) (for 1h at room temperature). As negative control, primary antibodies were omitted in which case no signals were detected (data not shown). Nuclei were stained with hematoxylin or DAPI (Vector Laboratories). Pictures were taken using a Leica DM5500 (epifluorescence) microscope (Leica Microsystems, Wetzlar, Germany). Proportions of immunoreactive cells were counted in at least 3 replicates using Fiji software (https://imagej.net/ImageJ).

Array comparative genomic hybridization (array CGH)

Organoids were harvested from Matrigel and genomic DNA from the organoids and primary tumors isolated using the Purelink Genomic Mini Kit (Invitrogen), according to the manufacturer's instructions. Array CGH analysis was done using the 8x 60K CytoSure ISCA v3 microarray (Oxford Gene Technology). Genomic DNA was labeled with Cy5 for 2h using the CytoSure Labelling Kit and hybridized to Cy3-labeled sex-matched reference DNA for at least 16h at 65 °C in a rotator oven (SciGene). Arrays were washed using Agilent wash solutions with a Little Dipper Microarray Processor (SciGene) and scanned using an Agilent microarray scanner (2 µm resolution), followed by calculation of signal intensities using Feature Extraction software (Agilent Technologies). Quality control and data analysis were performed using CytoSure Interpret Software and circular binary segmentation algorithm.

Exome and whole-genome sequencing and downstream analysis

Tissue and organoid DNA libraries were prepared with the KAPA Hyper Prep kit (Kapa Biosystems) and the whole-exome was captured by the SureSelect Human All Exon V7 Captured kit (Agilent). Whole exome Libraries were sequenced at 30X coverage on an Illumina Nextseq generating 2x151bp reads and low coverage whole genome libraries were sequenced on an Illumina HiSeq4000 (single-end 51 bp reads) up to a depth of 0.1-0.2x coverage.

Raw sequencing reads were aligned to the human reference genome GRCh38 with Burrows-Wheeler Aligner (BWA) (Li and Durbin, 2009), duplicates were removed and the base quality score was recalibrated following Genome Analysis Toolkit (GATK)4 best practices. We obtained an average sequencing depth of 74x (range: 46 - 100) and over 90% of the exome was covered over 10x (Table S4). Variants were called with MuTect2 and further annotated with Annovar (Wang et al., 2010). Common variants present in the 1000 genome project, exome sequencing project (ESP6500), Haplotype Reference Consortium (hrcr1), kaviar database (version 20150923), exome aggregation consortium (exac03) and gnomad (v211) database were filtered out. All remaining indels and substitutions uniquely present in the tumor or corresponding organoids were manually reviewed in the Integrative Genome Viewer (IGV) resulting in 1638 mutations (Table S3).

The low-coverage whole-genome sequencing data were also mapped with BWA to the hg19 reference genome resulting in on average 17,937,065 mapped reads (range: 6,133,741- 48,816,522) (Table S4) and processed with QDNAseq (Scheinin et al., 2014) and ASCAT (Van Loo et al., 2010). The resulting segments and their LogR values per bin of 30kb are used to create the copy-number profiles per sample. The tumor cell fraction (%) and corresponding ploidy was estimated with ASCAT (Van Loo et al., 2010) using the whole-genome sequencing data.

The raw data from low-coverage whole-genome sequencing and whole-exome sequencing are available in the ArrayExpress database at EMBL-EBI (www.ebi.ac.uk/arrayexpress) under accession number E-MTAB-8636 and E-MTAB-8637, respectively.

Targeted Sanger sequencing

Specific primers (Table S5) were designed to amplify the targeted *BRCA1* gene region by PCR using primary tumor and organoid genomic DNA and the Phusion DNA polymerase kit (New England Biolabs). The amplicon was verified using gel electrophoresis, purified with the Invitrogen purification kit (Thermo Fisher Scientific) according to the manufacturer's protocol, and Sanger-sequenced by Eurofins Genomics (Ebersberg, Germany).

Gene expression analysis by RT-qPCR

RNA was extracted from organoids using the RNeasy Micro Kit (Qiagen) according to the manufacturer's instructions. RNA concentration and quality were analyzed with the Nanodrop Spectrophotometer. cDNA was synthesized using the Superscript III First-Strand Synthesis Supermix (Thermo Fisher Scientific) and subjected to SYBR Green-based quantitative real-time PCR (qPCR) with the StepOnePlus Real-Time PCR System (AB Applied Biosystems) and gene-specific forward and reverse primers designed with PrimerBank (https://pga.mgh.harvard.edu/primerbank/) and PrimerBLAST (https://www.ncbi.nlm.nih.gov/tools/primer-blast/) (Table S5). Primer validation was done using melting curve analysis and gel-electrophoresis (data not shown). Expression levels were normalized to expression of the housekeeping gene glyceraldehyde-3-phosphate dehydrogenase (*GAPDH*). Relative gene expression levels were calculated as ΔCt values (Ct 'target gene' minus Ct '*GAPDH*') and the corresponding heatmap generated by Heatmapper (http://www2.heatmapper.ca/expression/).

Drug screening

Organoids were harvested from Matrigel and dissociated into single cells using TrypLE (supplemented with ROCKi) and mechanical dispersion. The cell suspension was resuspended in 70% Matrigel/30% OCOM4 and 2000 cells/3 µL drop were seeded per well of a 96-well plate. Culture medium was added and organoids were allowed to grow for 2-4 weeks. A concentration dilution series of paclitaxel

(Paclitaxel AB), carboplatin (Carbosin), doxorubicin (D1515, Sigma Aldrich), gemcitabine (Gemcitabine AB), nutlin-3 (Cayman Chemical) or vehicle (DMSO) control was applied to the organoid cultures (in triplicate). Cell viability was assayed after 72h of treatment using the XTT assay (X6493, Invitrogen) following the manufacturer's instructions (Invitrogen). Data analysis and determination of IC_{50} values was done with GraphPad Prism (Version 8.0.1).

Statistical analyses

Statistical analyses were performed using GraphPad Prism (Version 8.0.1) and are specified in the figure legends. Statistical significance was defined as $p < 0.05$. All experiments were performed with at least 3 biological replicates ($n \geq 3$; each including 2-3 technical replicates), unless otherwise indicated.

REFERENCES

Kopper, O., de Witte, C.J., Lõhmussaar, K., Valle-Inclan, J.E., Hami, N., Kester, L., Balgobind, A.V., Korving, J., Proost, N., Begthel, H., et al. (2019). An organoid platform for ovarian cancer captures intra- and interpatient heterogeneity. Nat. Med. *25*, 838–849.

Li, H., and Durbin, R. (2009). Fast and accurate short read alignment with Burrows-Wheeler transform. Bioinformatics *25*, 1754–1760.

Scheinin, I., Sie, D., Bengtsson, H., Van De Wiel, M.A., Olshen, A.B., Van Thuijl, H.F., Van Essen, H.F., Eijk, P.P., Rustenburg, F., Meijer, G.A., et al. (2014). DNA copy number analysis of fresh and formalin-fixed specimens by shallow whole-genome sequencing with identification and exclusion of problematic regions in the genome assembly. Genome Res. *24*, 2022–2032.

Van Loo, P., Nordgard, S.H., Lingjærde, O.C., Russnes, H.G., Rye, I.H., Sun, W., Weigman, V.J., Marynen, P., Zetterberg, A., Naume, B., et al. (2010). Allele-specific copy number analysis of tumors. Proc. Natl. Acad. Sci. U. S. A. *107*, 16910–16915.

Wang, K., Li, M., and Hakonarson, H. (2010). ANNOVAR: Functional annotation of genetic variants from high-throughput sequencing data. Nucleic Acids Res. *38*, 1–7.